TRANSIENT AND STEADY STATE LATERAL CHARGE TRANSPORT IN POLYMERIC SEMICONDUCTORS

A Thesis

submitted in partial fulfillment for the degree of

Master of Science

as part of the

Integrated Ph.D programme

(Materials Science)

By

ABHAY K. TIWARI

CHEMISTRY AND PHYSICS OF MATERIALS UNIT

JAWAHARLAL NEHRU CENTRE FOR ADVANCED SCIENTIFIC RESEARCH

BANGALORE – 560 064, INDIA.

MAY 2010

DECLARATION

I hereby declare that the matter embodied in this thesis entitled "**Transient and Steady State Lateral Charge Transport in Polymeric Semiconductors**" is the result of the investigations carried out by me at the Chemistry and Physics of Materials Unit, Jawaharlal Nehru Centre for Advanced Scientific Research, Bangalore, India under the supervision of Dr. N.S.Vidhyadhiraja and it has not been submitted elsewhere for the award of any degree or diploma.

In keeping with the general practice in reporting scientific observations, due acknowledgements has been made whenever the work described is based on the findings of other investigators.

Abhay Kumar Tiwari

Publications

(1) "**Transient and Steady State Lateral Charge Transport in Polymeric Semiconductors**" accepted for publication in **Optical and Quantum Electronics**.

CERTIFICATE

I hereby certify that the matter embodied in this thesis entitled "**Transient and Steady State Lateral Charge Transport in Polymeric Semiconductors**" has been carried out by Mr. Abhay Kumar Tiwari at the Chemistry and Physics of Materials Unit, JNCASR under my supervision and it has not been submitted elsewhere for the award of any degree or diploma.

Dr. N. S. Vidhyadhiraja
(Research Supervisor)
Theoretical Sciences Unit,
JNCASR

To My Late Grandfather

Acknowledgements

I cordially thank my research supervisor Dr. N. S. Vidhyadhiraja for giving me a nice research environment. He is a gentle supervisor, a responsible guardian, a friend, a great teacher and an excellent human being. His unmatched patience, sincerity, clarity in knowledge and dedication towards research has taught me a lot in life. I sincerely acknowledge all his support and care given to me during my tenure at JNCASR.

I would like to thank Prof. C. N. R. Rao, FRS for establishing JNCASR and Prof. M. R. S. Rao, President, JNCASR for giving excellent research environment.

I would also like to thank Prof. Umesh Waghmare under whom I have done my first research problem. His guidance during my summer project has given me a lot of confidence and the necessary threshold to do research. His warmhearted behaviour and deep knowledge in his area has always attracted me.

I sincerely acknowlege our collaborator and my course instructor Prof. K. S. Narayan. I thank him for various discussions. His inimitable scientific aptitude and support has always encouraged me.

I thank the coordinators of Integrated PhD Program, Prof. G. U. Kulkarni

and Prof. Balasubramanian for their constant encouragement and support.

I acknowledge Prof. S. Ranganathan, Prof. Chandrabhas Narayana, Prof. Swapan Pati, Dr. Subir Das, Dr.Jain, Prof. S. M. Shivaprasad, Prof. Sundaresan, Prof. Shobhana Narasimhan, Dr. Tapas Maji and Dr. M. Eswaramoorthy for the nice courses they offered and for their encouragement and support.

I acknowledge my lab mates Himadri, Pramod, Sudeshna, Dasari and Rukhsaan for making a vibrant atmosphere for research in lab. I thank them for all their support and encouragement.

I acknowledge all my Integrated PhD classmates Soumik, Piyush, Ritu, Nitesh, Urmi, Bivas, Nisha, Vini and Sekhar for all scientific and non-scientific support and encouragement. They have been excellent friends and have supported me in all ups and downs.

I acknowledge my JNC friends Mighfar, Anil, Hembram, Sandeep, Darshana, Prashant, Viswas, Prakash for their encouragement and support. I acknowledge my IISc Senior Rahul, Dipankar and Anupam and friends Akshaya, Vishwanath, Prabhat and Rahul for their encouragement and support. I acknowledge Raj Mohan (RRCAT Indore) for his valuable discussion on Kinetic Monte Carlo.

I thank complab staff for all sorts of help they have given during my research work. I also acknowledge Health Clinic Staffs at JNCASR Dr. Subba Rao, Dr. Kavita Sridhar and Dr. Archana for valuable medical consultancy. I acknowledge senior Administrative office A. N. Jaychandra, office and Canteen staffs. I acknowledge academic section and library staffs for their help.

I also thank professors of my alma-mater BHU for their encouragement and support.

Finally I would like to thank my parents and my younger brother Rahul whose constant support and affection has brought me at this stage.

Synopsis

This is a synopsis of the thesis entitled "**Transient and Steady State Lateral Charge Transport in Polymeric Semiconductors**" delivered by Abhay K. Tiwari of the Chemistry and Physics of Materials Unit, Jawaharlal Nehru Centre for Advanced Scientific Research, Bangalore, India. This thesis is divided into five chapters and three appendices.

(A)The first chapter is an overview of field of organic semiconductors. In this chapter I have discussed some of the basic properties of organic semiconductors, charge carriers in organic semiconductor devices and few models which have been used earlier by other groups to understand mechanism of the charge transport in organic semiconductors.

(B)The second chapter of this thesis is based on the spreading impedance model proposed earlier in our group[18,47]. In this thesis, the model has been solved in the time domain, and thus has helped us in carrying out the transient analysis and modulation frequency dependence. Through the simulations various aspects of transient analysis, effect of incident photocurrent, trapping and metal-semiconductor surface have been analyzed. Apart from the agreement with the existing experimental data and previous simulations, we have made a few new predictions, which await experimental confirmation.

(C) The third chapter is related to the analytical treatment of the spreading impedance model. This work describes the effect of different time-scales involved in the transients. A detailed analysis of the dependence of the lateral photovoltage on the different device parameters has been done. Using this analysis, we propose ways of optimizing the performance of organic devices.

(D) The fourth chapter has been devoted to the study of the mobilities of charge carriers in disordered organic semiconductors with the help of Kinetic Monte Carlo technique.

(E) In the fifth chapter the salient features of findings of the thesis has been summarized and some of the future plans have been discussed.

Contents

List of Figures

Chapter 1

Introduction

1.1 Introduction to Organic Semiconductors

Electronics in the present age is dominated by solid state devices based on inorganic semiconductors like silicon and germanium. A new paradigm is emerging rapidly in the form of organic semiconductors which could in principle even overshadow the presence of inorganic materials in the arena of microelectronics. Organic semiconductors span the areas of physics, chemistry, materials science and engineering. The main adavantages that they offer over their inorganic counterparts are the potential for low cost, ease of fabrication, and unique properties such as flexibility and transparency along with the realization of new applications, such as large area, flexible light sources and displays, low cost printed integrated circuits or plastic solar cells.

The history of organic semiconductors is quite old. The first studies on organic semiconductors had been done on early 20th century of the dark and

photo-conductivity of anthracene crystals [1-3]. Later on with the discovery of electroluminescence in the 1960s[4] many researchers started investigation of molecular crystals. Thorough research started on understanding the phenomena of optical excitation and charge carrier transport. Finally in 1970s the successful synthesis and controlled doping of conjugated polymers established the organic semiconductors[5-7]. Heeger, MacDiarmid and Shirakawa received Nobel Prize in Chemistry in 2000 for *the discovery and development of conductive organic polymers* [5]. Later on the development of organic semiconductors was enhanced due to the development of organic photovoltaic cell [7-11], thin film transistors [12-15] and in last few years there has been a revolution due to the display technology based on the organic light emitting diodes [16-18].

1.2 Basic Properties of Organic Semiconductors

Organic semiconductors differ from inorganic semiconductors in the optical properties, band structure, charge carrier transport and device operations. We briefly discuss here some of the aspects.

1.2.1 Optical Properties

Since there is weak electronic delocalization in organic molecular solids the luminescence spectra is similar to the gas phase or in solution [19]. In the spectra of organic semiconductors there exists well-defined spin states (singlet

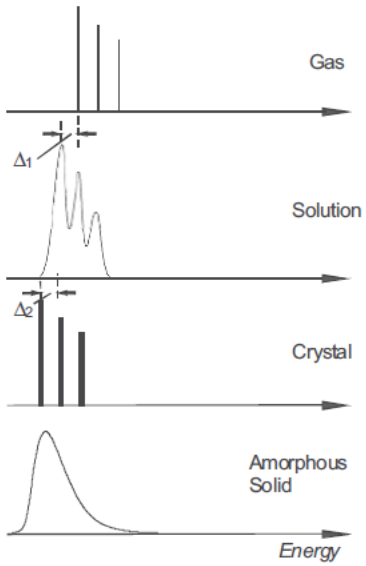

Figure 1.1: Optical spectra of organic molecules in different surroundings(ref. 1)

and triplet) and hence have important consequence on the various physical properties like quantum efficiency. Another important optical property of organic semiconductors is that optical excitations are localized to a single molecule. They have an energy gap typically between 1.5 eV to 3.0 eV.

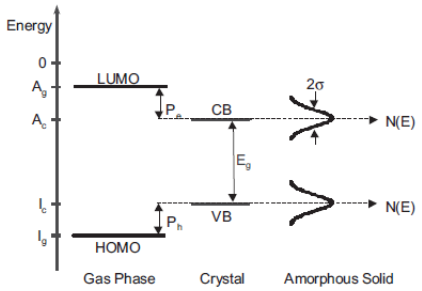

Figure 1.2: Band Structure and density of states in organic semiconductors(ref. 1).

1.2.2 Band Structure

The band structure is strongly dependent on morphology and the structure. In organic semiconductors, molecular orbitals combine to form Highest Occupied Molecular Orbital (HOMO) and Lowest Unoccupied Molecular Orbital (LUMO) rather than continuous band structure in other solids[19]. For charge transport, a crude analogy can be made between LUMO and valence band and HOMO and conduction band. Since organic semiconductors are disordered solids, so their energies are Gaussian distributed. We can see in the figure 1.2 that density of states in organic semiconductors is Gaussian.

1.3 Materials Overview

Molecular Materials used in organic semiconductor devices are either low molecular weight molecular solids or conjugated polymers. Both have in common a conjugated π-electron system. In conjugated polymer devices morphology and structure are also important factors and generally the band gap of these materials can be tuned according to desired characteristics by controlling these factors. The main polymers used in organic electronic devices industry are (i) Poly(2-methoxy-5-(2- ethylhexyloxy)-1,4-phenylene vinylene) (MEHPPV), (ii) Poly(3-hexylthiophene) (P3HT) and (iii) Poly(9,9-dioctylfluorene-alt-bithiophene) (PFO TT)[17]. Some more polymers used for electronics application are shown in figure 1.3.

1.4 Charge carriers in Organic Semiconductors

The charge carriers in conjugated polymer have been interpreted in terms of self-localized excitations or photo-induced excitations. These excitations gives rise to the formation of quasi-particles. The charge transport in organic semiconductors is mainly due to (i) solitons [20-21], (ii) polarons [22], (iii) bipolarons [23] and (iv) excitons.

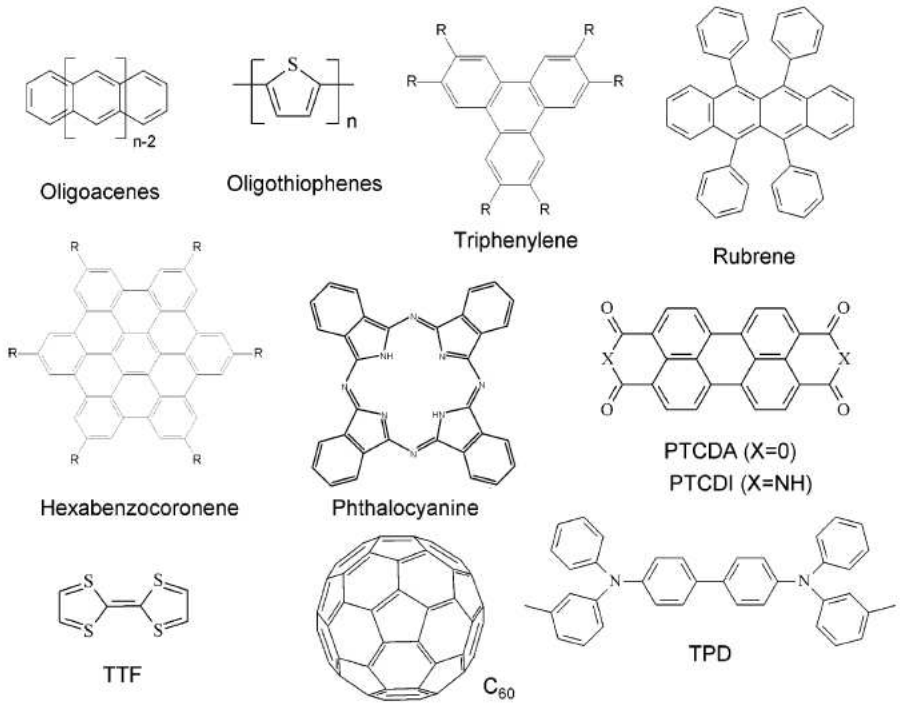

Figure 1.3: Various Polymers used for Optoelectronic application(ref. 17).

1.4.1 Solitons

A self-reinforcing solitary wave like a wave packet or pulse that maintains its shape, travels at constant speed and is caused by a cancellation of non-linear and dispersive effects in the medium is called a soliton. In polymers, solitons are self-localized nonlinear localizations. This phenomena is related to weakly lifted ground state degeneracy. Polymers offered a nice system to study topological solitons[20-21].

In conjugated polymers due to sp^2p_z hybridization, the π band is half filled, which can lead to metallic conductivity. Since there is strong intra-chain coupling and a weak interchain coupling the electrons are confined to a linear chain and hence makes polymers a quasi-one dimensional conductor. There occurs modulation along the chain due to strong tendency to distortion of these quasi-one dimensional metals[24-25]. Peierl's Theorem [79] state that within the mean field approximation the ground state of quasi-one-dimensional is spontaneouly distorted to form a charge density wave with period $\frac{2\pi}{Q} = \frac{2\pi}{2k_f}$ where k_f is the Fermi wave number. The schematic diagram of a soliton has been shown in figure 1.4.

1.4.2 Polarons

A polaron is a fermionic quasiparticle composed of a charge and its accompanying polarization field [25]. In the polymer, when charge is introduced the charge carriers are self trapped causing deformation in the chain(figure 1.5).

This deformation accompanied by the excess charge carriers leads to the

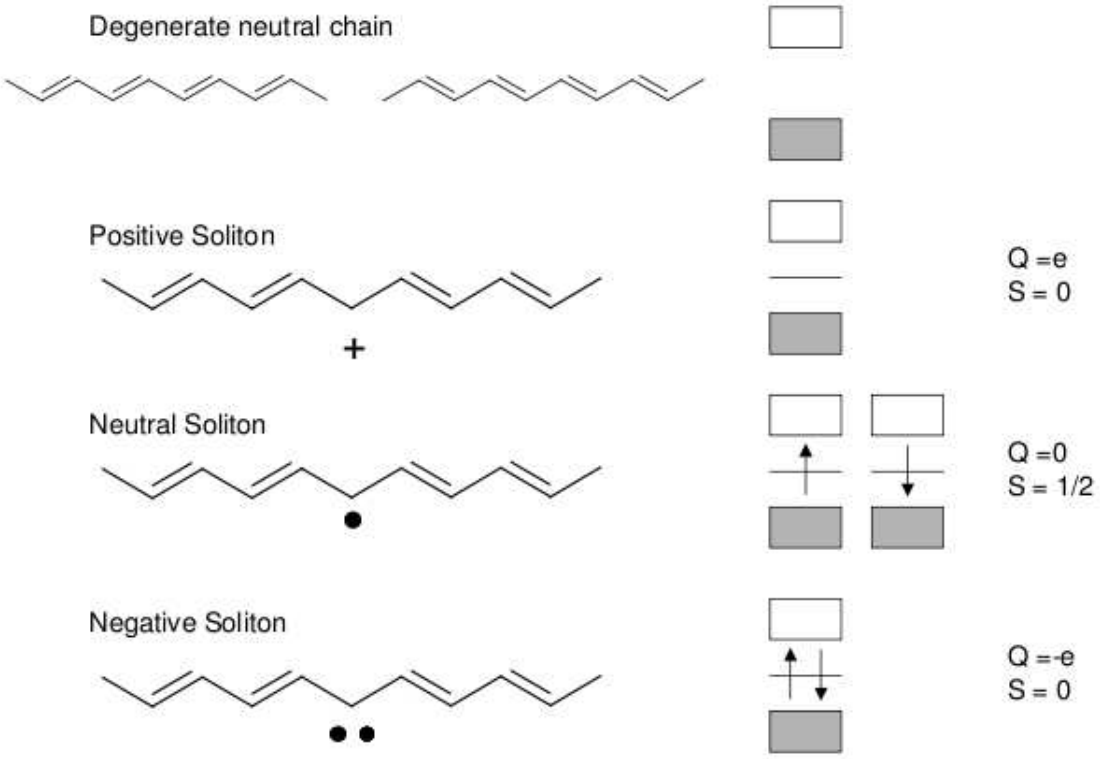

Figure 1.4: Schematic diagram of solitons for various spin and charged states(ref.80).

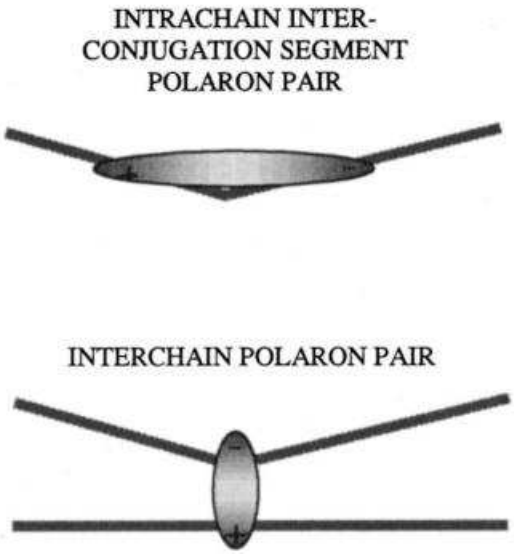

Figure 1.5: Polaron in intermolecular chain and in intramolecular chain(ref.79).

generation of polaron. Polaron contributes to the charge transport via hopping in non-degenerated and degenerated conjugated polymers [26].

1.4.3 Bipolarons

When two polarons come close and form a spinless and doubly charged quasi-particle, it is termed as a bipolaron(figure 1.6) [26]. Stability of bipolarons depends on temperature and charge concentration of carriers. At low charge or high temperature bipolarons can dissociate into two polaron.

1.4.4 Excitons

An Exciton is a quantum of electronic excitation energy travelling in the periodic structure of a crystal. It is neutral and its movement across the

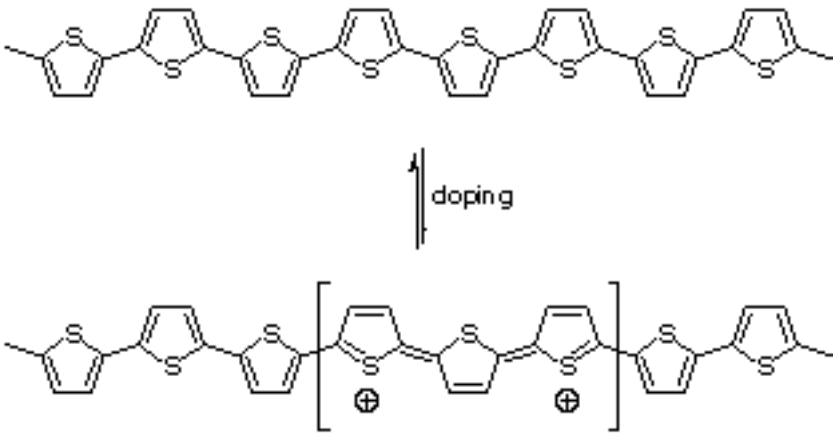

Figure 1.6: Bipolarons in Polythiophenes.

solids causes the transportation of energy. Excitons can be formed by association of free carriers or by direct photoexcitaion. Upon photoexcitation, charge carriers are formed and binding leads to the formation of excitons (electron-hole pair). Excitons are evident in conjugated polymers, semiconducting single-wall carbon nanotubes, semiconducting quantum dots[27,28].

Excitons played a key role in the photovoltaic and light emitting diode applications. They have an important role in superconductivity and in the transport of energy in biological system [28]. Excitons are generally of three types:

Frenkel Excitons

In materials with small dielectric constant, the coulomb interaction between electron and hole tends to be strong and the size of excitons tend to be small comparable to size of the unit cell (figure 1.7). These excitons are called Frenkel Excitons. Frenkel excitons have large oscillator strengths for electronic transition. They have binding energy between 0.1 to 1 eV.

Wannier-Mott Excitons

Wannier-Mott excitons have larger radius than Frenkel excitons covering some hundreds of atomic sites(figure 1.7). The energy expression for Wannier-Mott excitons is same as that of Hydrogen atom.

$$E_n = E_\infty - \frac{R}{n^2} \tag{1.1}$$

where $n = 1, 2, \ldots$ is the principal quantum number and $R = \frac{me^4}{2h^2\epsilon^2}$. Here m,e, h and ϵ is the effective mass, electronic charge, Planck's Constant and dielectric constant respectively. Wannier-Mott excitons are more common in inorganic semiconductors. The binding energy ranges from several meV to 60 meV.

Charge Transfer Exciton

Charge transfer exciton is an intermediate state exists between the excitons formed upon light absorption and the free charges in the ground state leads to formation of a charge transfer exciton[29]. Charge Transfer Exciton are in between Wannier-Mott and Frenkel exciton(figure 1.7).

1.5 Modeling Charge Transport in Organic Semiconductors

One of the main challenges in Organic Semiconductors for device operation is to know about the charge transport. There are various models employed to study the charge carriers in Organic Optoelectronic devices but still nothing can be said to well established and the quest is still on to know about

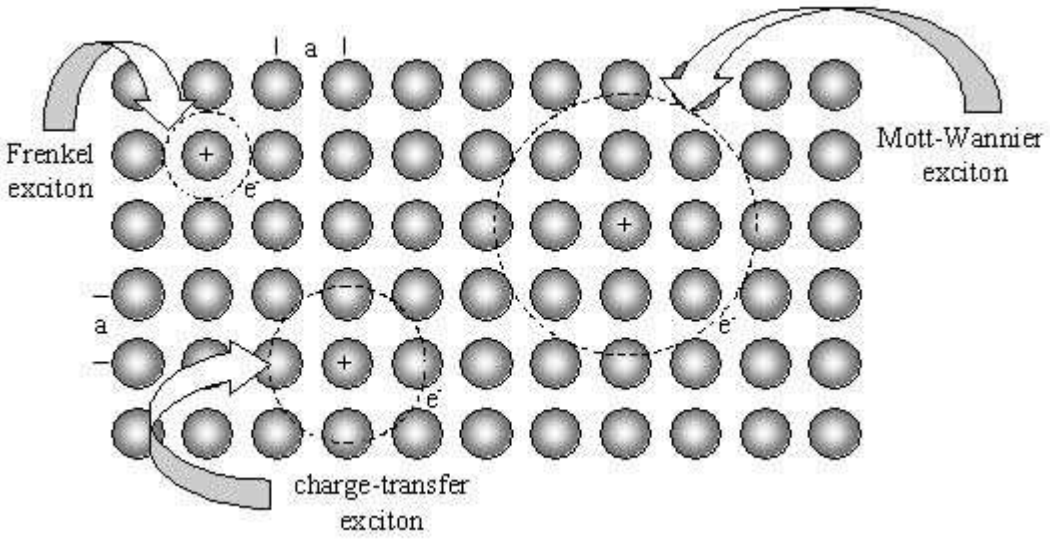

Figure 1.7: Sketch showing various types of excitons.

the charge carrier dynamics in organic semiconductor devices. Since polymers are disordered solids, they pose challenge for theory in explaining how chemical composition, geometric structure, and packing affect in the transport properties. To model organic semiconductors generally there are two approaches: (a) Molecular Approaches; (b) Macroscopic Approaches. Here are some models which are generally used.

1.5.1 Molecular Approaches

Molecular approaches gives insight for electronic and structural properties of two dimensional sheets of conjugated polymers. Quantum Chemical calculations are used to calculate the rate of charge transfer between two molecules[30-35]. Ab-initio calculations are highly accurate in determining the parameters that govern the rate of charge transfer.

In the semiconducting polymers, HOMO (for hole transport) and LUMO (for electron transport) are spatially delocalized due to large overlap of the partially filled π-level. The rate of charge transfer is defined by the strength of the coupling between frontier orbitals. These coupled orbitals of molecules leads to the delocalization of charge across the two molecules. Conversely, when the molecules are poorly coupled, the charge is strongly localized on a single molecule and only able to transfer to the other molecule via a thermally assisted hop.

Quantum Chemical calculations are based on Kohn Sham Hamiltonian[36] given below.

$$\mathcal{H}^e = \mathcal{T}^k + V_{ee} + V_{ext} \tag{1.2}$$

where $\mathcal{T}^k$ is the kinetic energy of electrons, V_{ee} is the electron-electron repulsion term and V_{ext} is the external potential. V_{ext} can also be defined in terms of local potential $v_{ext}(r)$ as $V_{ext} = \int dr \rho(r) v_{ext}(r)$ where ρ is the charge density.

Now when a charge hops from a molecule $M_1(\theta_x^{M_1})$ to another molecule $M_2(\theta_x^{M_2})$ the initial and final electronic wave functions can be written as

$$\begin{aligned} \phi_i &= A|\theta_1\theta_2\theta_3 \ldots \theta_x^{M_1} > \\ \phi_f &= A|\theta_1\theta_2\theta_3 \ldots \theta_x^{M_2} > \end{aligned} \tag{1.3}$$

where $\theta_1\theta_2\theta_3 \ldots \theta_{x-1}$ are the one electron wavefunctions of other electrons which do not move during charge transfer and A is normalization constant.

It is also called " frozen orbital approximation".

Now the hopping rate J_{if} and and reorganizational energy δE is calculated

$$J_{if} = \langle \theta_x^{M_1} | \mathcal{H}^e | \theta_x^{M_2} \rangle \tag{1.4}$$

$$\delta E = \langle \theta_j^{M_2} | \mathcal{H}^e | \theta_j^{M_2} \rangle - \langle \theta_i^{M_1} | \mathcal{H}^e | \theta_j^{M_1} \rangle \tag{1.5}$$

Despite the evident usefulness of such a molecular approach it has certain limitations due to the requirement of large scale computation. It can about the properties of single molecules very well but the intermolecular charge transfer rates cannot be related directly to the charge mobility at device level. The latter depends on the intermolecular rates between many molecules, across large length scales. More details can be found in reference 78.

1.5.2 Green's Function Method

A Green's function, $G(x, s)$, of a linear differential operator $L = L(x)$ acting on distributions over a subset of the Euclidean space R^n, at a point s, is any solution of

$$LG(x, s) = \delta(x - s) \tag{1.6}$$

where δ is a Dirac Delta function [37]. Green's functions have been used to solve inhomogeneous differential equations subjected to certain boundary conditions [40]. In conjugated polymers the dynamics of charge carriers are described by a kinetic equation known as master equation. The master

equation is given by

$$\frac{\partial f_i(t)}{\partial t} = -\sum_{j\neq i} W_{ji} f_i(t)[1 - f_j(t)] + \sum_{j\neq i} W_{ij} f_j(t)[1 - f_i(t)] - \lambda_i f_i(t) \quad (1.7)$$

where $f_i(t)$ is the occupational probability of the site at position R_i and energy E_i at time t. The transition time from site j to site i is described by rate W_{ij} and the decay process is taken into account through the rates λ_i [41]. This master equation is nonlinear and very difficult to handle in general. The Green's function method can be used to solve the linearized master equation as discussed next. At low intensities due to low occupational probabilities equation 1.7 gets linearized to

$$\frac{\partial f_i(t)}{\partial t} = -\sum_{j\neq i} W_{ji} f_i(t) + \sum_{j\neq i} W_{ij} f_j(t) - \lambda_i f_i(t) \quad (1.8)$$

The Laplace transform of the equation in matrix form may be written as

$$Rf = 0 \quad (1.9)$$

where f is a vector with elements f_i. The diagonal elements of the relaxation matrix R with

$$R_{ii} = p + \lambda_i + \sum_{j\neq i} W_{ji}. \quad (1.10)$$

and the off-diagonal elements by

$$R_{ij} = -W_{ij} \quad (1.11)$$

Now, the Green function $\mathcal{G}_{ij}(p)$ is defined as

$$\mathcal{G}(p)\mathcal{R}(p) = 1 \tag{1.12}$$

which can be written as

$$\mathcal{G}_{ij}(p) = \left(\delta_{ij} + \sum_{i \neq j} \mathcal{G}_{il}(p) W_{lj}\right) \mathcal{G}^0_{jj}(p) \tag{1.13}$$

where

$$\mathcal{G}^0_{jj}(p) = \frac{1}{p + \lambda_i + \sum_{i \neq \mu} W_{\mu j}} \tag{1.14}$$

The average luminescence intensity at time t is given by

$$L(t) = \left\langle \sum_i \lambda_i f_i(t) \right\rangle = \left\langle \sum_{i,j} \mathcal{G}_{jj}(t) \lambda_i f_i(t) \right\rangle \tag{1.15}$$

The Green's function formalism has the advantage of getting exact time dependent luminescence spectra with reasonable approximations. Various methods such as the percolation method and the continuous random walk method can be said to be special cases of the master equation approach.

1.5.3 Gaussian Disorder Model

Since organic solids are highly disordered, band theory is inapplicable for calculating charge mobilities. The charge transport mechanism in organic systems depends upon their morphology, order, and molecular structure. In such systems the energetic distribution of the highest occupied molecular

orbital (HOMO) and lowest unoccupied molecular orbital (LUMO) levels of the molecules can be well approximated by a Gaussian-like distribution [41]. Gaussian Disorder Model(GDM) is among one of the macroscopic models which explicitly takes all the factors into the account and has been found useful in for understanding and analysing experimental data [41-43].
GDM is employed by using Miller Abrahams expression along with Monte Carlo simulation. The Miller Abraham expression is given as follows:

$$\begin{aligned} \Gamma_{ij} =& \Gamma_0 \exp(-2\gamma_{if} R_{if}) \exp \frac{E_i - E_f}{K_B T} \qquad E_f > E_i \\ =& \Gamma_0 \exp(-2\gamma_{if} R_{if}) \qquad\qquad E_f \leq E_i \end{aligned} \tag{1.16}$$

where Γ_0 is the frequency pre-factor, γ_{if} constant describes the interaction between sites i and f, R_{if} is the distance separating centre of the two molecules, E_i and E_f are the energies of the charge on sites i and f respectively, k_B is the Boltzmann constant, and T is the temperature. Detailed explanation of the model has been given in chapter 4 and in reference 41.

1.5.4 Equivalent Circuit Models

Equivalent Circuit Models are phenomenological model that have been widely used in explaining device characteristics like I-V curves and external voltage dependence in solar cells, etc. In this approach we model the phenomena in terms of basic circuit elements like resistance, capacitance and diode[44-46]. By using Kirchhoff's laws we can get the circuit equations. Circuit models gives us a better hold on the macroscopic parameters involved in device operations. They can help immensely in predicting some new features of

the devices and device geometry. However, the disadvantage with the circuit models is that they are mostly device specific and can't be generalized. But if coupled with other models like the GDM, they lead to a lot of exciting results.

1.6 Scope of the Thesis

In this thesis, we have modeled an organic position sensing device with an Spreading Impedance Model that was proposed by our group previously [46]. Along with this, we have also predicted some features which could be helpful in increasing sensitivity of the device. A detailed analytical analysis has been carried out and this yields deeper insight into the muliple time scales involved in the charge transport. In later part of the thesis we have simulated the GDM with Kinetic Monte Carlo and again we benchmark our numerical implementation with well known physics such as the Poole-Frenkel effect.

Chapter 2

Spreading impedance model: formulation and applications

The lateral photovoltaic effect (LPE) has been used as an effective tool to probe the dynamics of photogenerated charge carriers in conjugated polymer based optoelectronic devices. In this chapter, we analyze the time-dependence of LPE in a position sensing device geometry using a discrete circuit equivalent model coupled with a spreading impedance approach. The highlight of our analysis is that we are able to get not only the spatial but also the temporal evolution of the lateral potentials, charge density, and the lateral photovoltage (LPV). We elucidate the dependence of the lateral photovoltage (LPV) on the position, intensity and the modulation frequency (ω_c) of the light beam. Previous experimental results for the position and ω_c dependence of the LPV in the steady state are successfully reproduced within the present approach. We predict a clear knee-like feature in the transient regime of the LPV for high photocurrent values. This feature prompts

us to propose that the response time of the organic position sensing device decreases sharply with increasing incident intensity.

2.1 Introduction

Conjugated polymer based organic semiconductors have been explored extensively in optoelectronic applications as they offer tremendous advantages in processing and fabricating procedures. The lateral photovoltaic effect (LPE) has been used to probe the photogenerated charge carrier dynamics in optoelectronic devices [47,18]. Whereas a great deal of attention has been paid to the LPE in conventional inorganic semiconductors, LPE as a tool to investigate the charge dynamics in organic semiconductors is still not well established. In earlier work from our group(46), a spreading impedance approach [52] to a discrete circuit equivalent model was found to provide an excellent description of the experimental results in the steady state of a polymeric position sensing device. However, the analysis carried out in that work had certain limitations. The equations were linearized and solved in the frequency domain. Further, the Fourier frequency was equated to the modulation frequency of the incident light beam. So the limitations resulting from such an analysis are three-fold: The first and foremost being that transient dynamics information could not be obtained. Such studies are very important in understanding experiments such as time-of-flight measurements [49-51]. Secondly, linearization of the equations imply that non-linear effects that could arise at higher incident intensities etc cannot be observed; and

finally comparison to experiments could be carried out only for the spatial dependence of the LPV and for relatively low light intensities.

In this work, we have taken a different route for analyzing our model that lets us overcome all the three limitations mentioned above. We study the model directly in the time domain without linearizing the equations. This helps us to get the spatiotemporal dependence of the lateral transport within a single framework. Further, in previous work, the recombination effects across the Schottky diode back contact were treated in the linear regime. Such an approximation is naturally incorrect at high incident light intensities. In this work, this limitation has also been overcome, thus yielding specific predictions for the non-linear response of the device.

2.2 Model and formalism

2.2.1 Position Sensing Device

A **Position Sensitive Device**(PSD) and/or **Position Sensitive Detector** is an optical position sensor (OPS), that can measure a position of a light spot in one or two-dimensions on a sensor surface [55,56]. PSDs are used to electronically monitor the position or movement of a mechanical component. PSDs detect the movement and position of the control device and translate that movement and position into a control signal that may be further processed and used to control the movement of a vehicle or equipment.

A non-uniform light beam incident on PSD will generate a photocurrent

which flows from the incident point through the resistive and capacitive layers to the electrodes. By knowing the difference of the voltages between the two electrodes we can know infer the position of the light beam. The performance of PSDs depends on the linearity, sensitivity, and resolution of the response.

Recently there has been interest in using organic semiconductors as the active layer in a position sensing device due to its advantages in fabricating and processing. Organic PSDs have also been helpful in getting insight of length and time scales involved in the organic optoelectronic devices [46,48]. Our model is inspired by such a PSD fabricated in our collaborator Prof. K.S. Narayan's Group [48]. Through our model we have tried to get the position, modulation frequency and morphology dependence of the response of the device and to understand the length and time scales involved in organic optoelectronic devices.

2.2.2 Photophysics of Lateral Photovoltaic Effect

As mentioned above, in a PSD the incident light creates a photocurrent and the impedance forms a current divider that splits the current between two terminals, allowing the position of the spot to be determined by voltage differences between the two laterally separated electrodes. A schematic diagram of the device is given in figure 2.1.

The device structure consists of a polymer-Al Schottky junction with front pair of Au electrodes. The polymer used were poly(3-hexylthiophene)(P3HT) and poly-[2-methoxy,5- (2-ethylhexoxy)-1,4-phenylene vinylene](MEHPPV).

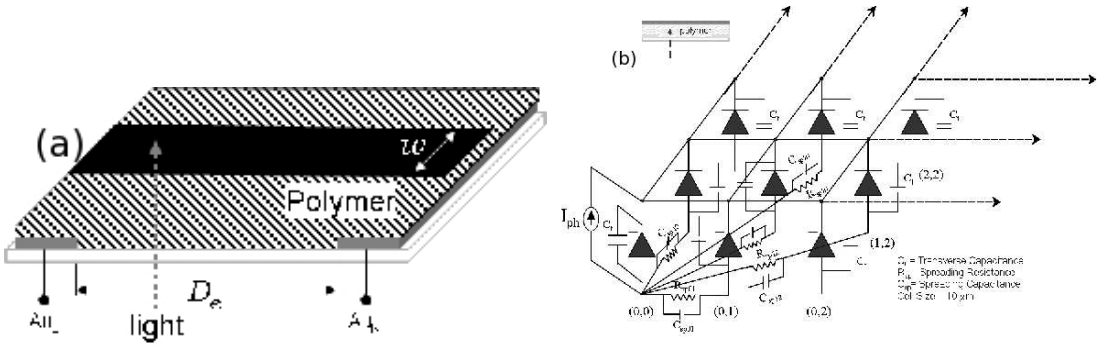

Figure 2.1: (a) Typical position sensing device (PSD) structure with polymer-Al Schottky junction of width W, and two front Au electrodes separated by distance D_e. (b)Equivalent circuit spreading impedance network model of the polymeric Schottky device(reference 18,47).

The lateral photovoltage is measured across the Au electrodes.

The incident light beam leads to the following sequence of events. Initially on photoexcitation the generation of excitons takes place. These excitons diffuses in the polymer matrix. At the proximity of metal-semiconductor interface where there is built-in Schottky-type barrier potential, these excitons get dissociated. Subsequently, the minority carriers (electrons) are transferred to the equipotential Al electrode, leaving the majority carriers (holes) in active polymer network. The separated holes at the interface distort the built-in potentially locally, which in the steady state sets up a non local lateral electric field that self consistently induces a lateral flow of the separated holes. This lateral charge flow produces a potential drop between the locus of illumination and the electrodes and thus a non-zero lateral photovoltage is developed.

2.2.3 Model

With the above picture of the physical phenomena involved in the device functioning a model has been developed. In the model since the lateral dimensions are much greater than the thickness of the sample, it has been assumed that the transverse gradient of potential is neglegible. The lateral potential profile $\phi_{ph}(r)$ is then discretized onto a square lattice of nodes, each node element m represented by a potential ϕ_m. The current through each node may be divided into a by a lateral and a transverse component. The circuit diagram showing discretization of the device structure using circuit elements in a 2D polymer matrix network interfaced with Al is given in fig 2.1.

(A) The transverse currents through the node , m has been modeled as a combination of a diode and a capacitive current. The current associated with diode is reverse saturation current due to the re-injection of minority carriers made possible by the reduction of the Schottky barrier potential. The diode current is given by

$$I^T_{D,m} = I_s \left[exp\left(\frac{q\phi_m}{k_B T}\right) - 1 \right] \tag{2.1}$$

The capacitance is the junction capacitance of metal-semiconductor interface. The capacitive current is given by

$$I^T_{C,m} = C_t \frac{d\phi_m}{dt} \tag{2.2}$$

For the illuminated nodes, the photogenerated majority charge carriers represented by a current source $I_{ph,m}$ is added to the transverse current component. The magnitude of $I_{ph,m}$ depends on the locus and the beam profile in the medium and the quantum efficiency. Here we have assumed that there is constant beam intensity within a radius r_{beam} of the center of the beam for simplicity.

(B)The lateral current has two components: a resistive component I_R^L arising due to the disorder scattering of the charge carriers, and a capacitive component I_C^L which is attributed to the presence of traps that affect the mobility of the charge carriers. The resistive and capacitive component of the current from node m to n are given as:

$$I_R^L = \frac{\phi_m - \phi_n}{R_{sp}(m,n)} \tag{2.3}$$

$$I_C^L = C_{sp}(m,n)\frac{d(\phi_m - \phi_n)}{dt} \tag{2.4}$$

Modeling the spreading impedance Since in highly disordered systems like organic polymers, the number of scattering centres increase much more rapidly with the internode distance $r_{mn} = |r_m - r_n|$.

By empirical fitting [46,57] it was found that the spreading function comes out to be of the form.

$$g(r_{mn}) = exp\left[\left(\frac{r_{mn}}{\zeta}\right)^{\alpha}\right] \tag{2.5}$$

where α is the stretching exponent of the spreading function and ζ is the

length scale which is characteristics of the material under consideration. Using the above mentioned spreading function the internode resistance and capacitance are given as follows:

$$R_{sp} = R_s g(r_{mn}) \tag{2.6}$$

$$C_{sp} = \frac{C_s}{g(r_{mn})} \tag{2.7}$$

where R_s and C_s are the sheet resistance and sheet capacitance respectively. The inherent morphological disorder in polymeric systems implies that there must necessarily exist a distribution $P(l)$ of the persistence lengths, l.

$$exp\left[\left(\frac{r_{mn}}{\zeta}\right)^{\alpha}\right] = \int_0^{\infty} dl P(l) \exp(-\frac{r}{l}) \tag{2.8}$$

The ζ and α appearing in the equation could be the result of averaging of simple exponential function with weighted function $P(l)$. The form for $P(l)$ has not been studied. It is commonly assumed that the stretched exponential corresponds to a kind of universal behavior which is independent of the details of individual processes. This idea has stimulated the proposal of several universal mechanisms based either on hierarchically constrained dynamics or on parallel relaxation [54].

In polymers there are certain nanocrystalline domains and the charge carrier are transfered from one crystalline domains to another. Here we can see an analogy between the various network models. In complex networks used for communication purpose there are certain hubs and the information is passed from one hub to another hub.

The random network topology generator introduced in Waxman (1988) is a geographic model for the growth of a computer network. In this model the nodes of the network are uniformly distributed in the plane and edges are added according to probabilities that depend on the distances between the nodes. The nodes of the network are uniformly distributed in the plane and edges are added according to probabilities that depend on the distances between the nodes. Hence the random graphs are useful in getting the internode correlation so that we can treat it in the mean field manner[54].

Building up of the equations:

Now we have divided the set of nodes into four mutually exclusively sets depending on whether the node is illuminated or not, and whether it is a part of electrode or not.

(i) S_{IL}: set of nodes that are illuminated,

(ii) S_{NIL}: set of non-illuminated non-electrode nodes

(iii) S_{LE}: set of nodes coincident with left electrodes, and

(iv) S_{RE}: set of nodes coincident with right electrodes.

A straightforward application of the Kirchhoff's current law yields the potentials for all the nodes. The equations are as follows:

For dark or non-illuminated nodes, $m \in S_{NIL}$

$$I_s \left[exp\left(\frac{q\phi_m}{k_B T}\right) - 1 \right] + C_t \frac{d\phi_m}{dt} + \sum_{l \in S_{IL}} \left[\frac{\phi_m - \phi_l}{R_{sp}(l,m)} + C_{sp}(l,m) \frac{d(\phi_m - \phi_l)}{dt} \right] = 0 \tag{2.9}$$

For illuminated nodes, $l \in S_{IL}$,

$$I_s\left[exp\left(\frac{q\phi_l}{k_BT}\right)-1\right]+C_t\frac{d\phi_l}{dt}+I_{ph,l}+\sum_{\substack{m\in S_N\\ m\neq l}}\left[\frac{\phi_l-\phi_m}{R_{sp}(l,m)}+C_{sp}(l,m)\frac{d(\phi_l-\phi_m)}{dt}\right]=0 \tag{2.10}$$

All the nodes on the electrodes would be equipotential, thus for the left electrode potential Φ_L,

$$N_LI_s\left[exp\left(\frac{q\Phi_L}{k_BT}\right)-1\right]+N_LC_t\frac{d\Phi_L}{dt}+\sum_{\substack{m\in S_{LE}\\ l\in S_{IL}}}\left[\frac{\Phi_L-\phi_l}{R_{sp}(m,l)}+C_{sp}(m,l)\frac{d(\Phi_L-\phi_l)}{dt}\right]=0 \tag{2.11}$$

Similarly, for the right electrode potential Φ_R,

$$N_RI_s\left[exp\left(\frac{q\Phi_R}{k_BT}\right)-1\right]+N_RC_t\frac{d\Phi_R}{dt}+\sum_{\substack{m\in S_{RE}\\ l\in S_{IL}}}\left[\frac{\Phi_R-\phi_l}{R_{sp}(m,l)}+C_{sp}(m,l)\frac{d(\Phi_R-\phi_l)}{dt}\right]=0 \tag{2.12}$$

where N_L and N_R are the number of left and right electrode nodes respectively. By solving equation 2.9- 2.12 we can determine LPV (ΔV_{ph}) defined by

$$\Delta V_{ph}(l,t)=|\Phi_L-\Phi_R| \tag{2.13}$$

The advantages of the method adopted here over the previous work [46,48] is that we can not only capture the transient profile of the response but also the non-linearity by keeping the exponential form of the diode current, i.e by not linearizing the exponential.

In an earlier study from our group, the exponential in equations 2.9- 2.12 had been linearized, and converted them to linear equations using Fourier transform. Additionally, the equations were solved for a single frequency,

namely the modulation frequency ω_c. In this work, we do not make such approximations. The equations are directly evolved in time using a simple first order finite difference technique. The resulting equations may be cast into a matrix format which is then treated using sparse matrix routines. The dependence of the lateral photovoltage on the amplitude and the modulation frequency was investigated.

2.3 Numerical Approach

The numerical technique here we have used to solve the differential equations is finite difference technique. Firstly, we discretize the equations and then solve it first for illuminated nodes and then for the rest of the nodes. The resulting equations may be cast into a matrix format which is then treated using sparse matrix routines. After that LPV is calculated and stored with respect to time. The dependence of the LPV on the amplitude and the modulation frequency was investigated. The detailed algorithm has been explained in the appendix.

2.4 Results and discussion

2.4.1 Steady State Response

Since the method adopted in this work has been implemented for the first time, we would like to benchmark it with our previous method and verify that we do indeed reproduce the results obtained previously. In order to carry out the benchmarking we employ a dc incident photocurrent and plot the steady

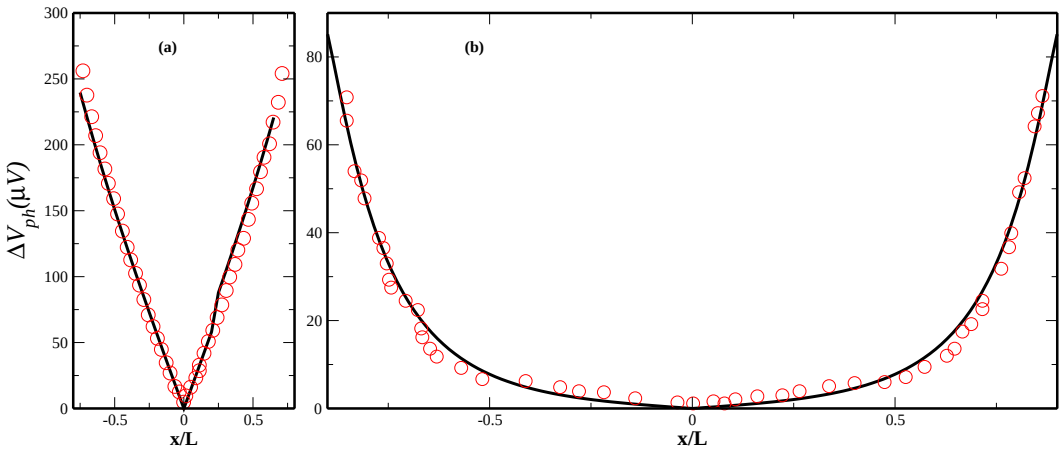

Figure 2.2: Steady state LPV *vs.* beam position.(a)$L/W \sim 1$ (b) $L/W \gg 1$. The solid line is the theory and circles are the experimental values for similar form factor devices(ref 18,47).

state lateral photovoltage as a function of the beam position in figure 1 for two devices of different form factors L/W. The other parameters such as the sheet resistance, junction capacitance, I_s and the spreading function parameters are the same as those in our earlier work. A direct superposition of theory onto the experimental results from [46,48] and a comparison to figures 2.2(a) and 2.2(b) shows that the present method does yield consistent results for the spatial profile of the LPV.

2.4.2 Transient Response

In what follows, we will consider a device with dimensions $0.7 \times 0.5\text{mm}^2$ implying a form factor $L/W = 1.4$, and focus on the transient response of the device to a dc as well as an ac incident photocurrent. In figure 2.3, the time dependent and normalized (with respect to its maximum value) LPV as a function of time for a dc incident light which is turned ON at t=0 and

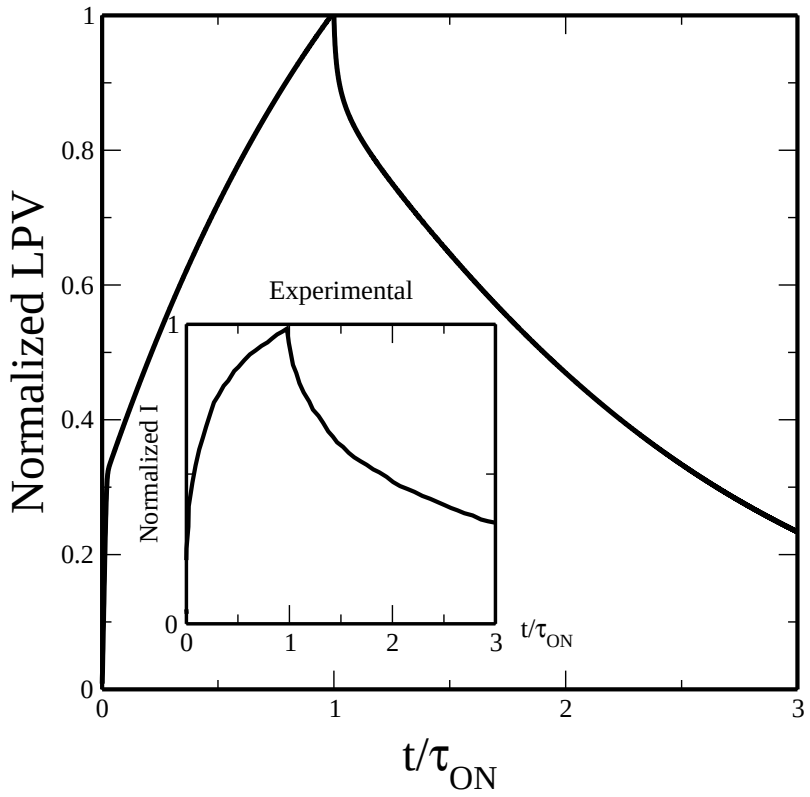

Figure 2.3: Transient On/Off Profile of the normalized LPV. In the inset is shown the experimentally measured photocurrent.

switched off at $\tau_{\rm ON} = 200$ seconds has been shown. The inset shows an experimentally measured $I_{ph}(t)$[46,48] between the two gold electrodes with one of the electrodes shorted with the *Al* electrode. The experiment employs an external load resistance to measure the output current, implying that the current is just proportional the LPV.

While there may be some contribution to the fall dynamics due to the trapping and detrapping of charges but we observe several unusual features in the experiment that are reproduced within the theory. We found that the photocurrent transients are not *RC* limited. Firstly, there is an obvious asymmetry between the rise and decay of the experimental LPV. A rapid

initial rise followed by a gradual rise (giving rise to the knee-like feature) is seen in experiment as well as theory. The decay is far more gradual than the rise, reflecting the interplay of various processes involving multiple time scales. The detail has been described in next chapter. We find that this asymmetry between the rise and decay occurs for high photocurrents ($\geq$ 10nA), and for $\tau_{\rm ON}$ that is comparable to the $t_{\rm knee}$. As explained below (figure 2.3)high photocurrents give rise to the knee-feature that reflects a very rapid rise. Switching off the incident light soon after $t_{\rm knee}$ gives rise to the slow decay.

2.4.3 Non-linear Response

We compute the LPV response to a series of increasing I_{ph} values to see if the functional form of the LPV and the time scales involved are dependent on the amplitude of the (dc) photocurrent. The result is shown in figure 2.4. We see that the time scales do depend significantly on the amplitude of the photocurrent. The saturation value of the LPV as a function of the incident photocurrent (inset, figure 2.4) shows a clear departure from linear response for larger I_{ph}. Such non-linearity is seen to manifest itself in the time-dependence of the LPV as well. A careful observation of the LPV(t) in figure 2.4(a) for higher I_{ph} shows a knee like feature, that is completely absent at low intensities.

In panel (b) of figure 2.4, we zoom on the knee feature, and show the LPV(t) for a few relatively high I_{ph} values. It is seen that this knee feature occurs earlier for higher I_{ph}. It is clear that this feature indicates that the

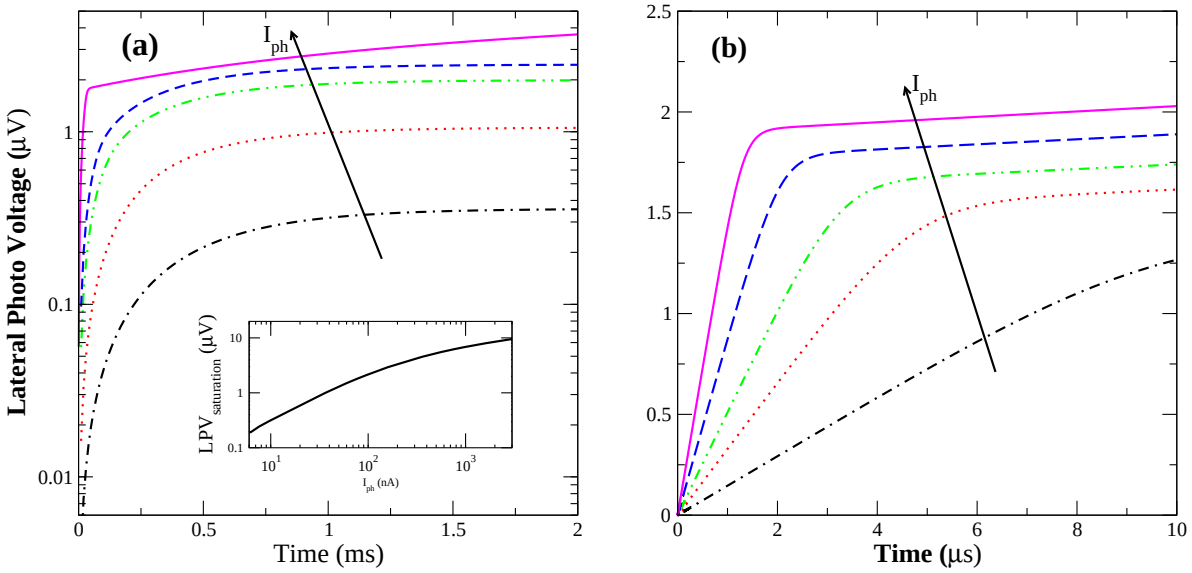

Figure 2.4: (a) Transient Values of the LPV as a function of different values of the incident photocurrent. The inset shows the LPV-saturation value as a function of the incident photocurrent. We can see a clear change in the slope. (b) Knee Voltage in the transient LPV is highlighted.

response time of the device decreases with increasing incident intensity. Note that the t_{knee} is of the order of microseconds, while the saturation occurs on a millisecond time scale (for the present set of parameters). This suggests that the initial rapid rise at high photocurrents could be utilized to obtain fast response in a polymeric Schottky diode device.

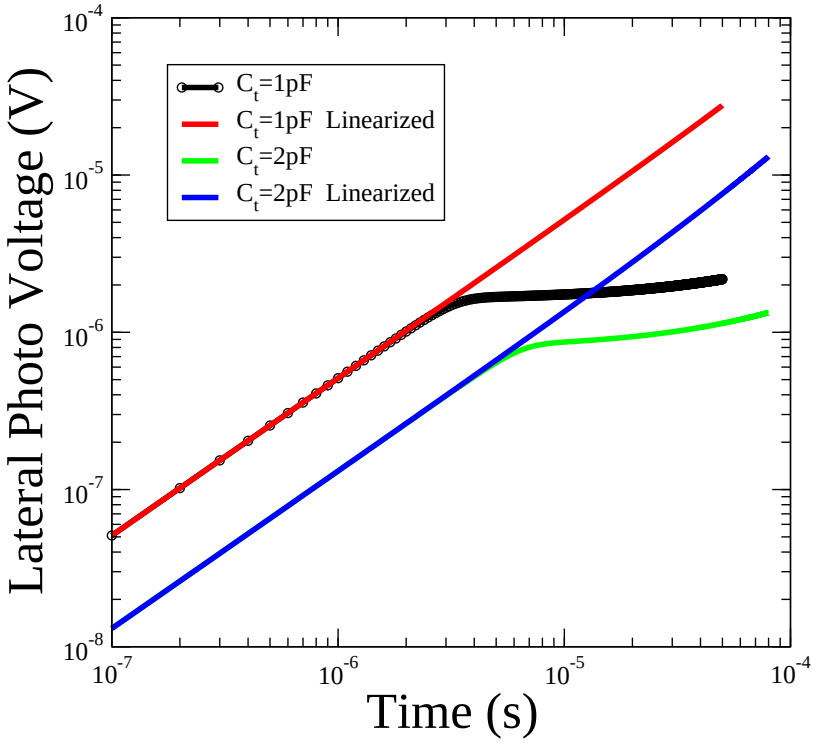

Figure 2.5: Non-linearity is due to the non-linear diode term. It is shown how the curves differ after t_{knee} when non-linearity is introduced.

Non-linearity in the transient response of LPV is due to the non-linear diode current. As we linearize the diode term there is no non-linearity in the transient response. In the figure 2.5 it is shown that how the curve the linearized equations do not yield the knee-like feature. The detailed analysis of non-linear nature has been given in the next chapter. We show the existence of at least two different time scales that are dependent on

incident photocurrent and reverse saturation current respectively and the wide separation between the two time scales is the factor responsible for the nonlinear features in the LPV.

2.4.4 Modulation Frequency Dependence

In this section we show the dependence of the steady state response (SSR) on the modulation frequency of the incident photocurrent. In figure 2.6 we show the maximum and the minimum of the SSR as a function of the modulation frequency. It is seen that the maximum of the SSR decreases sharply with increasing ω_c. This is seen in experiments as well [46,48] and thus provides further support to the theory presented here. In addition, the result shows that the maximum and the minimum converge to a common value at high frequencies. The insets show the actual LPV(t) for a relatively low ω_c and a high one.

2.4.5 Effects of Trapping and Metal-Semiconductor Interface

In this section we have studied the effects of trapping which has been modeled as sheet capacitance (C_{sh}) and the effect of Metal- Semiconductor interface which has been modeled as transverse capacitance (C_t). We can see in figure 2.7 that as we increase C_sh, LPV first rises to a value beyond its asymptotic($\rightarrow \infty$) value. As shown in figure 2.8, with the increase of C_t, not only does the maximum value of LPV increase but there is also shift in time at which the LPV attains the maximum. This unusual transient growth

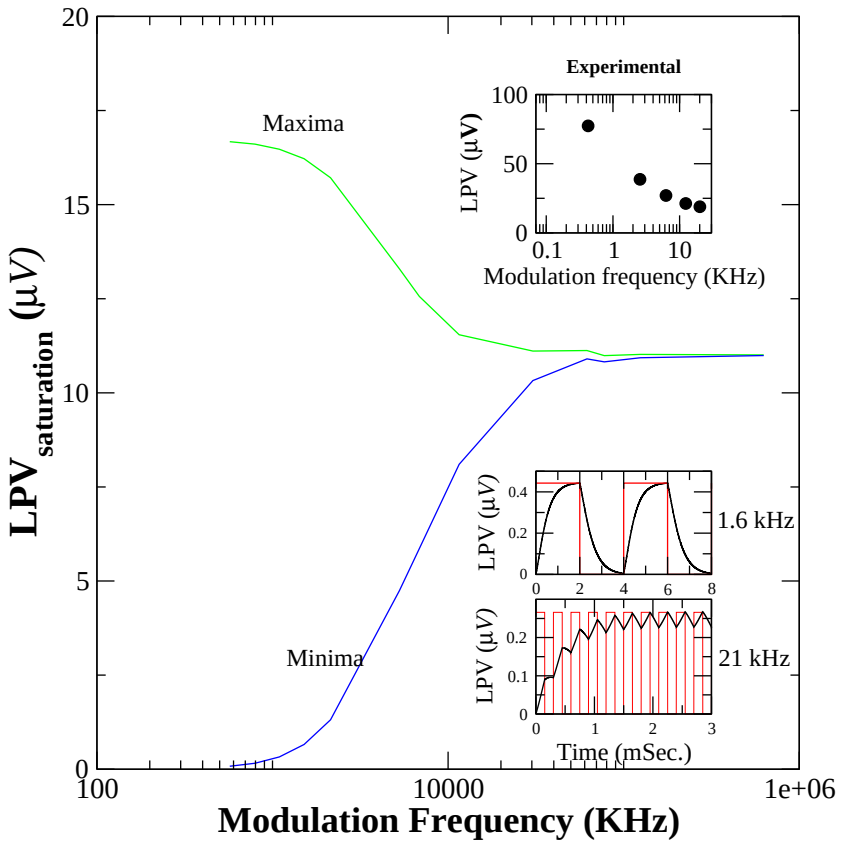

Figure 2.6: Maximum and minimum value of steady state response at various frequencies. In the upper set the experimental curve(ref. 18,47) is shown and in the lower ones the evolution of LPV(t) at a higher and a lower frequency.

behaviour leads us to the notion that both C_sh and C_t hold the key for the time scales involved in the organic semiconductor devices. Tuning of these parameters can help us in increasing the sensitivity of the devices. As we can see in the figure 2.7 that as we increase the C_{sh}, LPV first rises and then decays before saturating to a finite value.

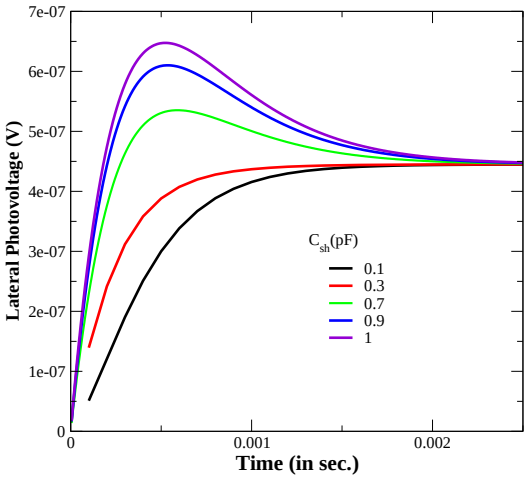

Figure 2.7: With the increase of the sheet capacitance the LPV first increases then decreases and saturates at a lower value than maximum rise.

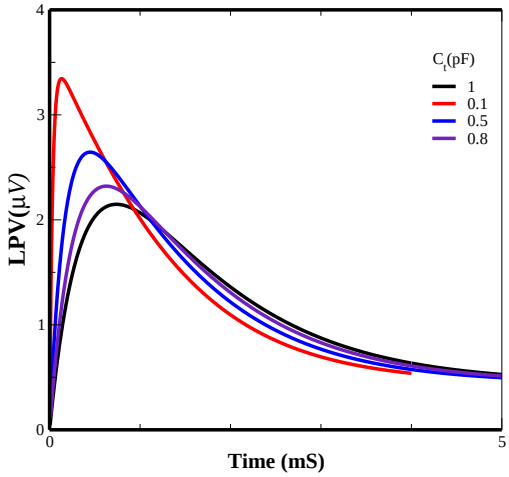

Figure 2.8: With the increase of transverse capacitance, not only does the the value of maximum LPV change but also shifted to lower time.

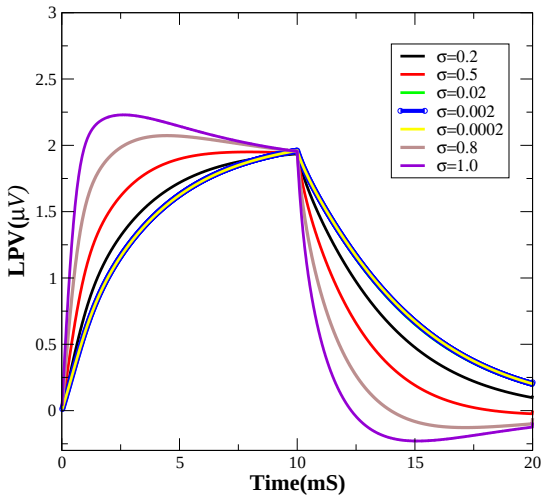

Figure 2.9: Disorder effects in the transverse capacitance.

2.4.6 Effects of Disorder

We have, until now, considered a single value of the transverse capacitance as well as the sheet impedances. However, real experimental devices cannot be expected to have a spatially uniform impedance profile. The Schottky interface, for example, would be quite disordered, and such disordered effects may be easily incorporated by considering a Gaussian distributed function for the transverse capacitance.Figure 2.9 shows the effect of varying disorder strength in C_t on the LPV. The changing profiles shows that as we increase the disorder there is considerable change in the rise and decay of the transients. Thus disorder can increase the transient profiles significantly(figure 2.9).

2.5 Conclusion

In this work, we present a consistent framework for exploring the transient and non-linear characteristics of lateral transport in organic polymeric devices. The theory presented here is benchmarked against earlier theoretical and experimental results. The agreement is seen to be quite good. We make a few predictions as well that can be tested by further experiments. One of them is the knee-like feature that is purely a non-linear response of the device to high photocurrents. The second is the deviation from linearity of the steady state LPV as a function of photocurrent. Further experimental investigations to test these predictions are presently going on in our group. We are also extending the theory further to make quantitative comparisons to experiment as well as investigate the effect of other parameters such as beam profile, morphology, junction capacitance and trap densities.

Chapter 3

ANALYTICAL SOLUTIONS

The previous chapter deals with the numerical solution of the equations that determine the two-dimensional potential profile resulting from a non-uniform illumination of an organic PSD. We observed several features of the transient and steady state potentials. Some of the more prominent and unusual features are the non-linearity of the steady state lateral photovoltage for $L/D \gg 1$, the knee feature in the rise part of the LPV and rise and then saturation of transients with respect to changing trap states (C_{sh}) and metal-semiconductor interface (C_t).

We showed that several of these features are in good agreement with experiments. However, physical understanding could not be achieved to a satisfactory level. In this chapter we re-examine the equations from an analytical perspective. With certain assumptions derived from the numerical solution, we make simplifications in the equations. These simplifications allow us to find the closed-form solution of the PSD equations in several cases, notably that of the steady state, and high modulation frequencies.

The analytical treatment of the model has enabled us to know the various time scales involved. Additionally, it has given us insight regarding how the parameters which play role in determining the sensitivity and the response of the device are associated with the time scale. The analytical treatment along with numerics has always been proved to be advantageous in time-based-modeling of carrier transport[58-59]. This practice is helpful in revealing the physical meaning of the parameters used in the equation.[60-61]

3.1 Solution of the equation when light is ON

3.1.1 Solution for the illuminated node

The equation for illuminated node potential ϕ_l is given by (see equation 2.10 of previous chapter)

$$I_s\left[exp\left(\frac{q\phi_l}{k_BT}\right)-1\right]+C_t\frac{d\phi_l}{dt}+I_{ph,l}+\sum_{\substack{m\in S_N\\ m\neq l}}\left[\frac{\phi_l-\phi_m}{R_{sp}(l,m)}+C_{sp}(l,m)\frac{d(\phi_l-\phi_m)}{dt}\right]=0 \tag{3.1}$$

The equation in its present form is difficult to solve because it involves the time dependence of all the other node potentials. The numerical solution of the equations show that the illuminated node voltage is far larger in magnitude than all the other nodes. Thus, as a first approximation, we drop all spreading impedance effects and get

$$I_s\left[exp\left(\frac{q\phi_l}{k_BT}\right)-1\right]+C_t\frac{d\phi_l}{dt}+I_{ph,l}=0 \tag{3.2}$$

Rearranging the equation we get

$$\frac{d\phi_l}{dt} + \alpha \exp\left(\frac{q\phi_l}{k_B T}\right) - \gamma = 0 \tag{3.3}$$

where

$$\alpha = \frac{I_s}{C_t} \quad , \beta = \frac{q}{K_b T} \quad , \gamma = \alpha\left(\frac{I_{ph,l}}{C_t} + + I_s\right) \text{ and } \; u = \beta\phi_l \tag{3.4}$$

It is important to note here that the only parameters that determine the ϕ_l are the thermal energy $k_B T$ and the combination of $\beta\alpha$ and $\beta\gamma$. Since $\beta\alpha$ and $\beta\gamma$ have units of inverse time and u is dimensionless, we denote $\beta\alpha = \tau_2^{-1}$ and $\beta\gamma = \tau_1^{-1}$ so the equation for $\beta\phi_l$ becomes

$$\frac{du}{dt} + \frac{e^u}{\tau_2} - \frac{1}{\tau_1} = 0 \tag{3.5}$$

Even at this level of approximation, we see that when the light is incident, the transients are governed by two time-scales, τ_2 and τ_1 where $\tau_2 = \dfrac{C_t}{\beta I_s}$ and $\tau_1 = \tau_2(\dfrac{I_{ph,l}}{I_s} + 1)^{-1}$. In general, $\dfrac{I_{ph,l}}{I_s} \gg 1 \Rightarrow \tau_1 \ll \tau_2$. This implies that there are two well separated time scales in the problem when the light is ON. When the incident light is OFF($I_{ph,l} = 0$) the two time-scales coincide hence $\tau_2 = \tau_1$ and the decay is governed by a single time-scale. Thus, we see that there is in general a marked asymmetry between the rise and decay of the photovoltage. The solution of the equation is simple and is given by (with initial condition $\phi_l = 0$)

$$\phi_l(t) = -\frac{1}{\beta}\ln\left[\frac{\alpha}{\gamma} + \left(1 - \frac{\alpha}{\gamma}\right)\exp\left(-\beta\gamma t\right)\right] \tag{3.6}$$

As $t \to \infty$ $\phi_l(t)$ reaches the saturation value.

$$\phi_l(t \to \infty) = \frac{-1}{\beta} ln \frac{\tau_1}{\tau_2} = \frac{1}{\beta} ln \frac{\tau_2}{\tau_1} \tag{3.7}$$

Let us define a timescale t_{knee} as the time it takes for ϕ_l to reach a large fraction $p(\to 1)$ of its saturation value, so

$$\phi_l(t_{knee}) = p\phi_l(\infty) \tag{3.8}$$

In practice, we take $p \approx 0.95 - 0.99$. Then the t_{knee} is given by

$$t_{knee} = -\tau \ln\left[\frac{\left(\frac{I_s}{I_{ph}}\right)^p - \frac{I_s}{I_{ph}}}{1 - \frac{I_s}{I_{ph}}}\right] \tag{3.9}$$

In Figure 3.1, we show a comparison between the simulated value and the analytically calculated illuminated node potential. After getting the analytical expression for illuminated node potential, we can now solve the electrode node equations and subsequently we can get the expression for LPV.

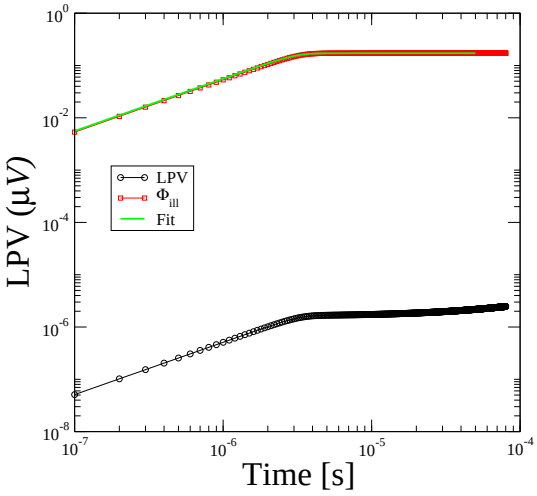

Figure 3.1: Lateral Photovoltage, Illuminated Node potential and the analytical fit has been shown. It can be clearly observed the illuminated node potential saturates when the LPV reaches the knee potential. Analytically calculated illuminated node potential is seen to agree spectacularly well with the simulated curve.

The equation for left electrode is given as

$$N_L \left[I_s \left[exp\left(\frac{q\Phi_L}{k_B T}\right) - 1 \right] + C_t \frac{d\Phi_L}{dt} \right] + \sum_{\substack{m \in S_{LE} \\ l \in S_{IL}}} \left[\frac{\Phi_L - \phi_l}{R_{sp}(m,l)} + C_{sp}(m,l) \frac{d(\Phi_L - \phi_l)}{dt} \right] = 0 \tag{3.10}$$

Rearranging the terms and denoting

$$R_L{}^{-1} = \sum_{m \in S_{LE}} \frac{1}{R_{sp}(m,l)} \tag{3.11}$$

$$C_L = \sum_{m \in S_{LE}} C_{sp}(m,l) \tag{3.12}$$

we get

$$N_L(e^{\beta\phi_l} - 1) + \frac{C_t}{I_s}\frac{d\Phi_L}{dt} + \frac{\Phi_L - \phi_l}{I_s R_L} + \frac{C_L}{I_s}\frac{d}{dt}(\Phi_L - \phi_l) = 0 \tag{3.13}$$

We know from the simulations that $q\phi_L \ll k_B T$, hence we linearized the diode term and write finally

$$\frac{N_L C_t + C_L}{I_s}\frac{d\Phi_L}{dt} + \left(N_L\beta + \frac{1}{I_s R_L}\right)\Phi_L = y(t) \tag{3.14}$$

where

$$y(t) = \frac{\phi_l}{I_s R_L} + \frac{C_L}{I_s}\frac{d\phi_l}{dt} \tag{3.15}$$

We note that for our simulation parameters $N_L C_t \gg C_L$ and $\frac{I_s\beta}{C_t} \gg \frac{1}{R_L N_L C_t}$, hence we can write the equation above as

$$\frac{d\Phi_L}{dt} + \frac{\Phi_L}{\tau_2} = y(t) \tag{3.16}$$

This is a simple first order inhomogeneous equation, and the solution is

$$\Phi_L(t) = e^{\left(-\frac{t}{\tau_2}\right)} \int_0^t e^{\left(\frac{t'}{\tau_2}\right)} y(t')dt' \tag{3.17}$$

We note that $\Phi_L(t)$ is governed by two time-scales τ_2 and τ_1. The latter enters through y(t), which contains the illuminated node potential $\phi_l(t)$. Knowing from the figure 3.1 that ϕ_l saturates for $t \geq t_{knee}$, we can write the full

solution as

$$\Phi_L(t) = e^{\left(\frac{-t}{\tau_2}\right)} \int_0^{t_{knee}} e^{\left(\frac{t'}{\tau_2}\right)} y(t')dt' + \int_{t_{knee}}^{t} e^{\left(\frac{t'}{\tau_2}\right)} y(t')dt' \tag{3.18}$$

$$= e^{\left(\frac{-t}{\tau_2}\right)} \int_0^{t_{knee}} e^{\left(\frac{t'}{\tau_2}\right)} y(t')dt' + \tau_2 y_\infty \left(1 - e^{\frac{t-t_{knee}}{\tau_2}}\right) \tag{3.19}$$

This gives the saturation value $\Phi(t \to \infty) = \tau_2 y_\infty$

$$\Phi_L(t \to \infty) = \frac{\tau_2 \phi_l(t \to \infty)}{I_s R_R} \tag{3.20}$$

Thus, the LPV in steady-state is given by

$$LPV = \Delta\Phi = |\Phi_L - \Phi_R| = \frac{\tau_2 \phi_l(t \to \infty)}{I_s} \left| \frac{1}{R_L} - \frac{1}{R_R} \right| \tag{3.21}$$

Since R_L and R_R depends on the position of the light beam, it is obvious that the lateral photovoltage will also be a function of the beam position. The functional form of the LPV will depend on the spreading function that enters the effective resistances R_L and R_R, and thus will depend on the morphology of polymers. We can simulate the expression for LPV and the result is given in Figure 3.2. Here we can see how the LPV of the position sensing device comes out to be truly related to the position of light beam through R_L and R_R. We have plotted equation 3.21 in figure 3.2 for devices of different form factors. We found that the profiles of LPV matches qualitatively with the experiment and our earlier simulations. In this plot we can see how the linear response of the device is dependent on $\frac{l}{w}$ ratio. As $\frac{l}{w}$ increases the response of Lateral Photovoltage deviates from the linearity.

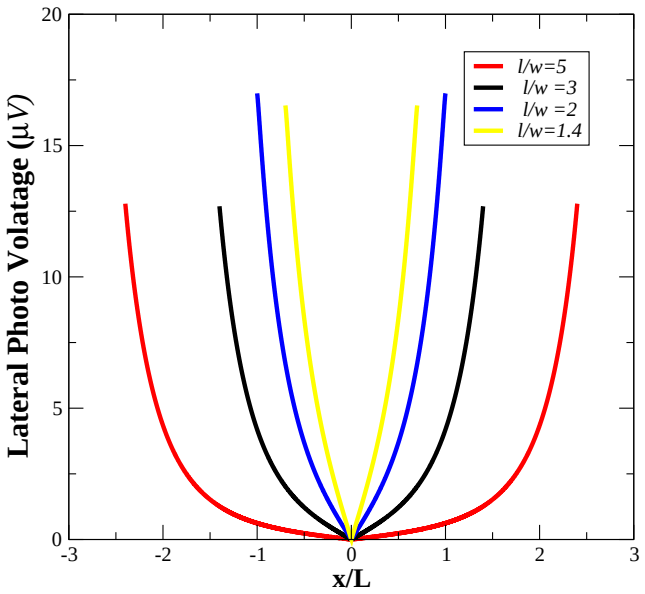

Figure 3.2: LPV calculated from the equation(3.21) for different $\frac{l}{w}$ ratios has been shown

3.2 Analysis of the LPV when the light is OFF

We envisage a situation when the light is incident for a certain time τ_{ON} and then it is switched off. The question that we ask is - how does the photovoltages decay ?

For the illuminated node equation 3.6 is solved again with $\tau_2 = \tau_1$ and initial condition $\phi_l(t = \tau_{ON}) = \phi_{lo}$. We get

$$\phi_l(t) = -\frac{1}{\beta} ln \left[\frac{\tau_1}{\tau_2} + \left(e^{\frac{\beta \phi_l}{\tau_{ON}}} - \frac{\tau_1}{\tau_2} \right) e^{-\frac{\tau - \tau_{ON}}{\tau_2}} \right] \tag{3.22}$$

Since $\tau_1 = \tau_2$,

$$\phi_l(t) = -\frac{1}{\beta} ln\left[1 + \left(e^{\frac{\beta\phi_l}{\tau_{ON}}} - 1\right) e^{-\frac{\tau-\tau_{ON}}{\tau_2}}\right] \tag{3.23}$$

The decay of $\phi_l(t)$ is seen from the above to be governed by τ_2. Thus, it is clear by comparing the rise and decay that the rise time scale is τ_1 while τ_2 governs the transient decay for the illuminated node.

The corresponding decay transient for the electrode nodes are

$$\Phi_L(t) = e^{-\frac{t}{\tau_2}} \left[\Phi_L(\tau_{ON}) e^{\frac{\tau_{ON}}{\tau_2}} + \int_{\tau_{ON}}^{t} e^{\frac{t'}{\tau_2}} y(t') dt'\right] \tag{3.24}$$

where

$$y(t) = \frac{1}{N_L C_t} \left(\frac{\phi_l}{R_L} + C_L \frac{d\phi_l}{dt}\right) \tag{3.25}$$

which is a function purely of $\dfrac{t - \tau_{ON}}{\tau_2}$.

Φ_R can be found by symmetry. Thus the picture become clear now.

In the rise profile of the illuminated node, the time scales that enters is τ_1, while in the decay, it is τ_2. Since $\dfrac{\tau_2}{\tau_1} = \dfrac{I_{ph,l} + I_s}{I_s} \gg 1$, the rise and decay of the illuminated node will always be asymmetric. However the effect of this asymmetry in LPV is subtle. Such an asymmetry will manifest itself in LPV only if τ_{ON}, the ON time of the incident light is close to or less than τ_1. This is because if τ_{ON} becomes of the order of τ_2, then the rise and decay profiles will be asymmetric. But if $\tau_{ON} \sim \tau_1$, then there will be a sharp rise (leading to the knee feature) but the decay will be very slow (given by τ_2). This is

indeed what we see in our simulations (figure 3.3).

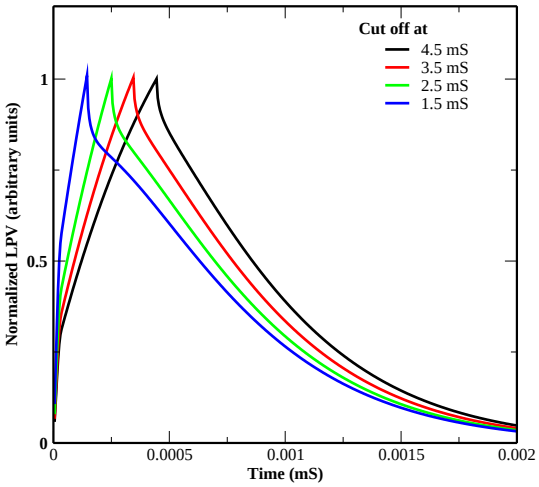

Figure 3.3: It is shown how the cut off time determines the decay of the LPV. When the light is turned OFF at time close to t_{knee} it decays slower.

It is seen that the ratio $\frac{I_{ph,l}+I_s}{I_s}$ governs the transient response.

3.3 Modulation Frequency Analysis

In previous sections, we have considered $I_{ph,l}$ to be just a step function, where it is on for $t \leq \tau_{on}$ and then switched off. Experimentally, one uses a modulated beam and a lock-in amplifier to extract the signal.

From the equation for $\phi_l(t)$ equation(3.2), it follows that

$$\frac{d\phi_l}{dt} + \alpha e^{\beta\phi_l} = \gamma(t) \tag{3.26}$$

where we have put

$$y = e^{\beta\phi_l} \quad \Rightarrow \quad y' = \beta e^{\beta\phi_l}\phi_l' \quad \Rightarrow \quad \phi_l' = \frac{1}{\beta y}y' \tag{3.27}$$

Now the equation become

$$\frac{y'}{\beta y} + \alpha y = \gamma(t) \tag{3.28}$$

$$\Rightarrow \quad y' + \alpha\beta y^2 = \beta\gamma(t)y \tag{3.29}$$

$$\Rightarrow \quad y' - \beta\gamma(t)y = -\alpha\beta y^2 \tag{3.30}$$

This has the form of Bernoulli's equation

Now,

$$u = \frac{1}{y} \quad \Rightarrow \quad u' = -y^2 y' \quad \Rightarrow \quad y' = -y^2 u' \quad = -\frac{u'}{u^2} \tag{3.31}$$

$$\frac{-u'}{u^2} - \frac{\beta\gamma(t)}{u} = -\frac{\alpha\beta}{u^2} \tag{3.32}$$

$$\Rightarrow \quad u' + \beta\gamma(t)u = \alpha\beta \tag{3.33}$$

To solve the differential equation first we calculate the integrating factor

$$\text{Integrating factor} = e^{\int f(t)dt} \tag{3.34}$$

$$u(t) = e^{-\left[\beta\frac{I_s - I_{ph}}{C_t}t + \frac{\beta I_{ph}}{\omega C_t}\sin\omega t\right]} \left\{ 1 + \alpha\beta \int_0^t e^{\left[\beta\frac{I_s - I_{ph}}{C_t}t' + \frac{\beta I_{ph}}{\omega C_t}\sin\omega t'\right]} dt' \right\} \tag{3.35}$$

where $u(t) = \exp(-\beta\phi_l(t))$ Now, we take $k = e^{-\left[\beta\frac{I_s-I_{ph}}{C_t}t+\frac{\beta I_{ph}}{\omega C_t}\sin\omega t\right]}$. Solving equation now,

$$u(t) = k\left\{1+\alpha\beta\int_0^t e^{\left[\beta\frac{I_s-I_{ph}}{C_t}t'+\frac{\beta I_{ph}}{\omega C_t}\sin\omega t'\right]}dt'\right\} \tag{3.36}$$

Here we take

$$I = \int_0^t e^{\left[\beta\frac{I_s-I_{ph}}{C_t}t'+\frac{\beta I_{ph}}{\omega C_t}\sin\omega t'\right]}dt' \tag{3.37}$$

expanding exponential we get

$$I = 1+\alpha\beta\int_0^t e^{\left(\beta\frac{I_s-I_{ph}}{C_t}t'\right)}\left(1+\frac{\beta I_{ph}}{C_t}\frac{\sin\omega t'}{\omega}+\cdots\cdots\text{higher order terms}\right)dt' \tag{3.38}$$

We would like to investigate the high frequency limit ($\omega_c \to \infty$), hence neglecting higher order terms in $\frac{1}{\omega}$

$$I = 1+\alpha\beta\int_0^t e^{\left(\beta\frac{I_s-I_{ph}}{C_t}t'\right)}dt'+\frac{\alpha\beta^2 I_{ph}}{\omega C_t}\int_0^t e^{\left(\beta\frac{I_s-I_{ph}}{C_t}t'\right)}\frac{\sin\omega t'}{\omega}dt' \tag{3.39}$$

$$= 1+\frac{\alpha C_t}{I_s-I_{ph}}e^{\left(\beta\frac{I_s-I_{ph}}{C_t}t\right)}+\frac{\alpha\beta^2 I_{ph}}{\omega C_t}\int_0^t e^{\left(\beta\frac{I_s-I_{ph}}{C_t}t'\right)}\frac{\sin\omega t'}{\omega}dt' \tag{3.40}$$

Now we consider the integral

$$I_1 = \int_0^t e^{gt'} \sin ht' dt' \tag{3.41}$$

solving by parts we get

$$I_1 = \frac{e^{gt}}{g} \frac{\sin ht - \frac{h}{g^2 e^{gt} \cos ht}}{1 + \frac{h^2}{g^2}} \tag{3.42}$$

Here $g = \dfrac{I_s - I_{ph}}{C_t}$ and $h = \omega$ Putting the values of the integral and k the final equation will be

$$\begin{aligned} u(t) =& e^{-\left(\beta \frac{I_s - I_{ph}}{C_t} t + \frac{\beta I_{ph}}{\omega C_t} \sin \omega t\right)} \left(1 + \frac{\alpha C_t}{I_s - I_{ph}} e^{\left(\beta \frac{I_s - I_{ph}}{C_t} t\right)}\right) + \\ & \frac{e^{-\left(\beta \frac{I_s - I_{ph}}{C_t} t + \frac{\beta I_{ph}}{\omega C_t} \sin \omega t\right)} \alpha \beta^2 I_{ph}}{\omega C_t} \left(\frac{e^{-\left(\beta \frac{I_s - I_{ph}}{C_t} t\right)}}{\frac{I_s - I_{ph}}{C_t}} \frac{\sin \omega t - \frac{\beta (I_s - I_{ph})}{\omega C_t}}{1 + \left(\frac{\beta (I_s - I_{ph})}{\omega C_t}\right)^2} \right) \end{aligned} \tag{3.43}$$

By cancellation of the terms and neglecting the terms with higher $\frac{1}{\omega}$ we get

$$u(t) = e^{\frac{I_s - I_{ph}}{C_t} t} + \frac{\alpha C_t}{I_s - I_{ph}} \tag{3.44}$$

So solution for $\phi_l(t)$

$$\phi_l(t) = \frac{1}{\beta} \ln \left(e^{\frac{I_s - I_{ph}}{C_t} t} + \frac{\alpha C_t}{I_s - I_{ph}}\right) \tag{3.45}$$

The equation for $\Phi_L(t)$ will be

$$\frac{d\Phi_L}{dt} + \left(\frac{I_s\beta}{C_t} + \frac{1}{N_R C_t R_L}\right. \Phi_L = \frac{1}{N_L C_t}\left(\phi_l(t) - \frac{d\phi_l}{dt}\right) \tag{3.46}$$

Putting the values of ϕ_l and $\frac{d\phi_l}{dt}$ we get

$$\frac{d\Phi_L}{dt} + \frac{\Phi_L}{\tau_2} = \frac{1}{N_L C_t}\left(\frac{1}{\beta}\ln\left(e^{(\frac{-\beta(I_s-I_{ph})}{C_t})} + \frac{\alpha C_t}{I_s - I_{ph}}\right) - \frac{(\frac{I_s-I_{ph}}{C_t})e^{-\beta\frac{I_s-I_{ph}}{C_t}t}}{e^{-\beta\frac{I_s-I_{ph}}{C_t}} + \frac{\alpha C_t}{I_s-I_{ph}}}\right) \tag{3.47}$$

The integrating factor is

$$e^{\int_0^t \frac{1}{\tau_2}dt'} = e^{\frac{t}{\tau_2}} \tag{3.48}$$

Now $\Phi_L(t)$ will be equal to

$$\Phi_L(t) = e^{\frac{-t}{\tau_2}}\int_0^t f(t)e^{\frac{t'}{\tau_2}}dt' \tag{3.49}$$

$$= e^{\frac{-t}{\tau_2}}\int_0^t \frac{1}{N_L C_t}\left(\frac{1}{\beta}\ln\left(e^{(\frac{-\beta(I_s-I_{ph})}{C_t})} + \frac{\alpha C_t}{I_s - I_{ph}}\right) - \frac{(\frac{I_s-I_{ph}}{C_t})e^{-\beta\frac{I_s-I_{ph}}{C_t}t}}{e^{-\beta\frac{I_s-I_{ph}}{C_t}} + \frac{\alpha C_t}{I_s-I_{ph}}}\right) \tag{3.50}$$

Breaking the integrals in two parts

$$I_1 = \int_0^t \frac{1}{\beta} \ln \left(e^{(\frac{-\beta(I_s - I_{ph})t'}{C_t})} + \frac{\alpha C_t}{I_s - I_{ph}} \right) e^{\frac{t}{\tau_2}} dt' \tag{3.51}$$

$$I_2 = \int_0^t \frac{(\frac{I_s - I_{ph}}{C_t}) e^{-\beta \frac{I_s - I_{ph}}{C_t} t}}{e^{-\beta \frac{I_s - I_{ph}}{C_t}} + \frac{\alpha C_t}{I_s - I_{ph}}} e^{\frac{t}{\tau_2}} dt' \tag{3.52}$$

Now

$$-\beta \frac{I_s - I_{ph}}{C_t} = a, \quad \frac{\alpha C_t}{I_s - I_{ph}} = b, \quad \frac{1}{\tau_2} = k \tag{3.53}$$

So we get

$$I_1 = \frac{1}{\beta} \int_0^t \ln (e^{-at'} + b) e^{kt'} dt' \tag{3.54}$$

Solving the equation by Mathematica, we get

$$I_1 = \frac{1}{\beta} \frac{1}{k^2(a+k)} \left\{ (a+k) e^{kt} (k \ln (e^{-at} + b) + a) \right\} - \frac{1}{\beta} \left[\frac{1}{k^2(a+k)} abk e^{t(a+k)} \ {}_2F_1(1, \frac{a+k}{a}, \frac{k}{a} + 2, -be^{ax}) \right] \tag{3.55}$$

$$I_2 = \frac{-\beta(I_s - I_{ph})}{C_t} \int_0^t \frac{e^{-at'}}{e^{-at'} + b} e^{kt'} dt' \tag{3.56}$$

$$= \frac{-\beta(I_s - I_{ph})}{C_t} \frac{e^{kt} \ {}_2F_1(a, \frac{k}{a}, \frac{k}{a} + 1; -be^{ax})}{k} \tag{3.57}$$

where ${}_2F_1$ is the confluent hypergeometric function. This can be further

simplified to give which leads to

$$\Phi_L(t) = e^{\frac{-t}{\tau_2}} \left\{ \frac{1}{\beta} \left[\frac{1}{k^2(a+k)} \left\{ (a+k)e^{kt} \times (k \ln (e^{-at}+b) + a) \right\} \right] \right\}$$
$$- e^{\frac{-t}{\tau_2}} \left\{ \frac{1}{\beta} \left[\left\{ (a+k)e^{kt} abke^{t(a+k)} \ {}_2F_1(1, \frac{a+k}{a}, \frac{k}{a}+2, -be^{at}) \right\} \right] \right\}$$
$$+ e^{\frac{-t}{\tau_2}} \left\{ \frac{-\beta(I_s - I_{ph})}{C_t} \frac{e^{kt} \ {}_2F_1(a, \frac{k}{a}, \frac{k}{a}+1; -be^{ax})}{k} \right\} \quad (3.58)$$

The asymptotic expansion of hypergeometric function ${}_2F_1(a', b', c', z)$ at $z \to \infty$ is given as

$${}_2F_1(a', b', c', z) = z^{-a'-b'} \left[z^b \frac{(-1)^{-a'}\Gamma(b'-a')\Gamma(c')}{\Gamma b'\Gamma(c'-a')} + \cdots \text{higher order terms} \right] \quad (3.59)$$

$$\approx \frac{(-1)^{-a'}\Gamma(b'-a')\Gamma(c')}{z^{a'}\Gamma(b')\Gamma(c'-a')} \quad (3.60)$$

In $\Phi_L(t)$, the second term may be neglected as it has $z^{a'}$ in the denominator which goes to zero as $z \to \infty$ Now putting the values we get

$$\Phi_L(t) = \frac{1}{N_L C_t} \frac{\tau_2^2}{\beta(\frac{\beta(I_s - I_{ph})}{C_t} + \frac{1}{\tau_2})} \left(\frac{1}{\tau_2} \ln (\frac{\alpha C_t}{|I_s - I_{ph}|}) + \frac{\beta(I_s - I_{ph})}{C_t} \right) \quad (3.61)$$

where

$$\frac{1}{\tau_2} = \frac{I_s \beta}{C_t} + \frac{1}{N_L C_t R_L} \quad (3.62)$$

Similarly,

$$\Phi_R(t) = \frac{1}{N_R C_t} \frac{\tau_2^2}{\beta(\frac{\beta(I_s - I_{ph})}{C_t} + \frac{1}{\tau_2})} \left(\frac{1}{\tau_2} \ln \left(\frac{\alpha C_t}{|I_s - I_{ph}|} \right) + \frac{\beta(I_s - I_{ph})}{C_t} \right) \quad (3.63)$$

And

$$\frac{1}{\tau_2} = \frac{I_s \beta}{C_t} + \frac{1}{N_R C_t R_L} \quad (3.64)$$

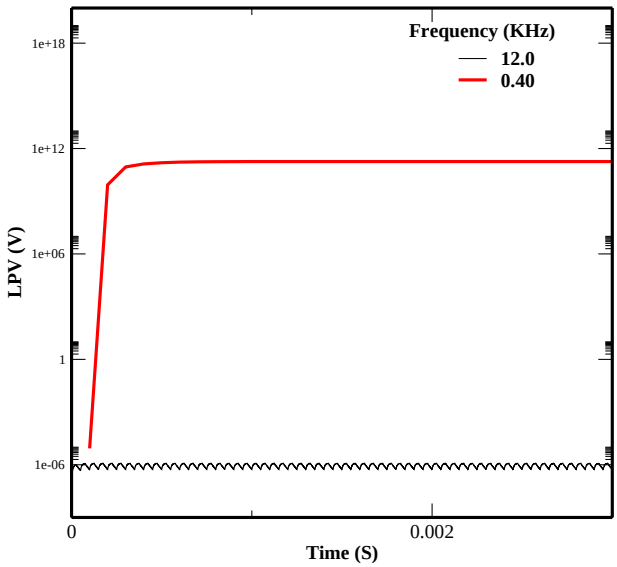

Figure 3.4: LPV as function of higher frequency and lower frequency

Here $N_L = N_R$ so $|\Phi_L(t) - \Phi_R(t)|$ depends on $\frac{1}{\tau_2}$ Now we can see from the frequency response curve given in the previous chapter that LPV reaches zero at higher frequency. Here also we can see that $|\Phi_L(t) - \Phi_R(t)|$ depends on τ_2.

As follows from the calculation that if $N_L = N_R$ then the $LPV \rightarrow 0$ at higher frequency. We can see from figure 3.4 as the value if $I_s = I_{ph,l}$ the

LPV reduces in order at high frequencies and can be approximated to zero. We can clearly see from the experimental curve (Figure 2.6) that at higher frequencies LPV approaches to zero.

3.4 Conclusion

Our analytical treatment of the model is quite helpful in not just knowing the existing feature of the devices but also predicting some new features. In this chapter we found that there are three different time scales involved that govern the device performance. The asymmetry involve in transients has been captured by the detailed analysis of incident photo-current and reverse saturation current. The LPV as function of beam modulation has also been studied and was found to be in good agreement with the experimental results. Thus, our analysis can be helpful for optimizing the performance of the devices.

Chapter 4

Charge Transport: A Kinetic Monte Carlo Approach

In this chapter I will be presenting study of charge carrier transport through a widely accepted Gaussian disorder model and Kinetic Monte Carlo approach. The mobility of charge carrier has been studied as a function of applied electric field and temperature.

4.1 Gaussian Disorder Model

In the introductory chapter a few aspects of the model have been described. The Gaussian Disorder Model is based the master equation which is derived from drift-diffusion equation and is given in equation 1.7. Now when the occupation probability is replaced by Fermi Dirac distribution

$$f_i = \frac{1}{1 + \exp\left(\frac{E_i - \mu_i}{K_B T}\right)} \tag{4.1}$$

Putting this into master equation, we can get Miller Abraham hopping rates. The GDM is based on the argument that charge-carrier transport occurs by hopping through a Gaussian density of transport states (DOS) of energetic widths.(Fig 1.1) Miller and Abrahams [75] were the first to calculate the hopping conductivity of semiconductors using reduced networks. Non-crystalline organic solids, such as molecular doped crystals, molecular glasses, and conjugated polymers, are characterized by small mean free paths for the carriers, as a result of the high degree of disorder present in the organic system. Therefore, the elementary transport step is the charge transfer between adjacent elements, which can either be molecules participating in transport or segments of a polymer separated by topological defects. These charge transporting elements are identified as sites whose energies are subjected to a Gaussian distribution

$$g(E) = \frac{N_t}{\sqrt{2\pi\sigma}} \exp\left(-\frac{E^2}{2\sigma^2}\right) \tag{4.2}$$

here E is the energy measured relative to the center of the density of states and σ is the standard deviation of the Gaussian distribution. Within this distribution, all the states are localized. With this technique, Time of Flight measurements can be simulated, in which mobility is derived from the mean arrival time of the carrier at the end of the sample and from their mean displacement. The predictions made concern the temperature and electric field dependence of the mobility.

4.2 Poole-Frenkel Effect

Poole Frenkel effect describes how insulators conduct electricity in the presence of large electric field [76-77]. As we know charge carriers in polymeric semiconductors are generally trapped in localized states. Some random thermal fluctuation will give the electron or hole enough energy to get out of its localized state, and move through the crystal, for a brief amount of time, before relaxing into another localized state. At higher electric field, the sufficient energy is provided by the electric field to pull out the carriers from a localized state. The expression for Poole-Frenkel effect is given as

$$J \propto E \exp\left(\frac{-q(\phi_B - \sqrt{\frac{qE}{\pi\epsilon}})}{k_B T}\right) \tag{4.3}$$

where J is the current density, E is the applied electric field, q is the elementary charge, ϕ_B is the potential barrier, ϵ is the dynamic permittivity, k_B is the Boltzmann's constant and T is the temperature.

For organic semiconductors, thermally assisted hopping mechanism is well described by Poole-Frenkel Effect. Understanding charge transport in organic semiconductors in large electric fields is relevant to many applications like field effect transistors, position sensing devices, solar cells and OLEDs and hence Poole-Frenkel effect turns out to be very helpful.

4.3 Kinetic Monte Carlo Simulation

Monte Carlo refers to a broad class of algorithms that solve problems by introducing randomness in the system. Metropolis Monte Carlo algorithm has been powerful technique in determining many physical properties of different types of systems. In the 1960s researchers began to develop a different kind of Monte Carlo algorithm for evolving systems dynamically from state to state[62]. After that there have been developments and applications of KMC in radiation damage annealing, in surface adsorption, diffusion and growth as well as in studying charge carrier dynamics in disordered organic semiconductors [63-70]. For the time-scales problem molecular dynamics (MD) are preferred choice. In MD one simulates the dynamical evolution of system of atoms using classical equations of motion. However, MD has a limitation that accurate integration requires time steps short enough to resolve the atomic vibrations. In this respect KMC is advantageous which attempts to overcome this limitation by exploiting the fact that the long-time dynamics of this kind of system typically consists of diffusive jumps from state to state[72-74].

The popularity and range of applications of kinetic Monte Carlo (KMC) has continued to grow and KMC is now a common tool for studying mobility in disordered organic semiconductors[41-43], the topic of this chapter.

4.4 Simulation and Results

We have also attempted to apply Kinetic Monte Carlo approach to study the charge carrier dynamics in disordered polymeric semiconductors. Our long term goal is to achieve a multi-scale model. This approach is an key step in this regard. The detailed algorithm is given in the Appendix but the simulation parameters and the results are described below.

For our computation we have selected $2\gamma a = 10$. Time has been normalized to $t_{ij}^0 = [6\gamma_0 \exp(-2\gamma a)]^{-1}$. $E = 1.1 \times 10^6 V/cm$ and $T = 400K$. We recorded position of the charge carrier with time and hence calculated the transit time. With the transit time we can get velocity using simple expression

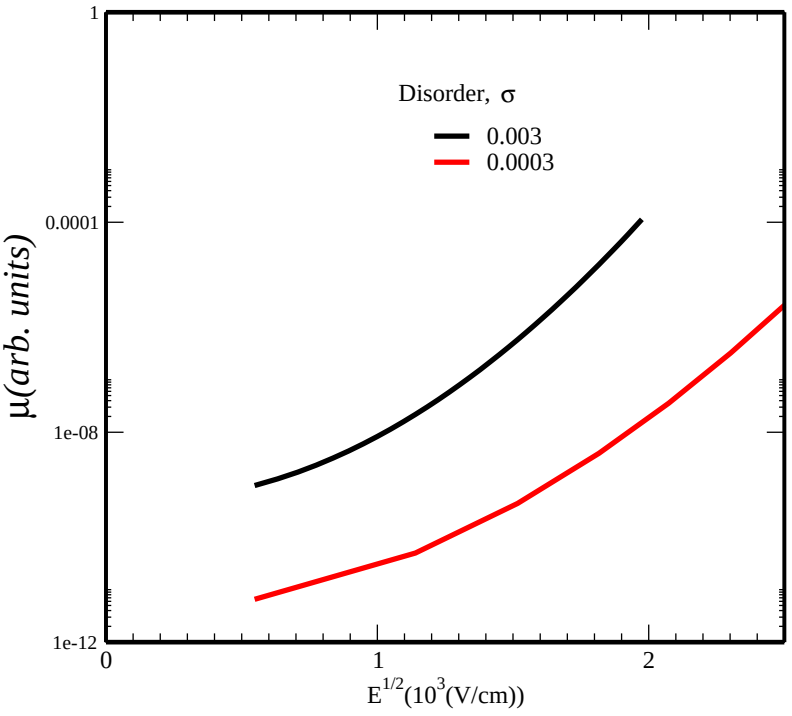

Figure 4.1: Mobility Vs Electric Field. It can be seen the curves are following Poole-Frenkel Effect at higher electric field

$$v = \frac{x}{t} \tag{4.4}$$

where v is the velocity x is the distance and t is the transit time. Mobility can be calculated as

$$\mu = \frac{v}{E} \tag{4.5}$$

where E is the electric field. After averaging over 150 carriers, the average mobilities was calculated. The mobilities with increasing field is calculated in the same manner and plotted. The plot is given in figure 4.1.

It can be seen in the plot that mobility follows the Poole- Frenkel effect. With the increasing electric field the mobility increases. However, by increasing the disorder the mobility should decrease, we have not been able to capture this feature yet. In general the mobility should decrease with disorder. As our simulations are in primary stage, we look forward to solve these ambiguities and to apply this technique in real devices.

4.5 Conclusion

Kinetic Monte Carlo is an effective method to describe the time of flight experiments. Our simulation is in preliminary stage and we look forward to achieve many more results in near future. We will be also looking to integrate spreading impedance model with KMC which can give many fold advantages.

Chapter 5

Summary

5.1 Summary

This thesis is focused on the modeling of the organic optoelectronic devices. Our model and its findings have been helpful in understanding the charge carrier dynamics and to know about the parameters governing the properties of device. The insights obtained can be helpful for the improvement of the devices and predicting new devices or new device geometries. Salient results of the thesis are as follows:

(A) Through our model and with our new numerical approach we have been successful in getting the steady state and transient properties of a position sensing device. The steady state and transient response does agree well with the experimental data. We have also been successful in explaining the modulation frequency response as well as the effect of trappping and metal-semiconductor interface on the performance of devices.

(B) We predict strong non-linearities in transient response of the device

at high incident intensities. This feature has not yet been reported in organic optoelectronic devices. If established experimentally it can be helpful in lowering the response time of the Organic PSDs.

(C) We have analyzed our model analytically. The analytical solution of our model has led us to better understanding of the model and phenomena involved. Not only has it supported our numerical simulations but also has given insight about the time scales involved in the system. The different time scales are controlled by different parameters. This approach has been of great help in optimizing device parameters for getting desired properties.

(D) We have also studied mobility of charge carriers with the help of well established Gaussian Disorder Model. Our simulation is in preliminary stage; however we have managed to simulate Poole-Frenkel effect.

5.2 Future Directions

In future, we will be extending our spreading impedance model to other device geometries. Apart from these, we are also looking ahead to integrate it with the KMC method. It will be interesting to incorporate quantum chemical methods also since it can help in dealing with the molecular level processes. Overall, we are looking forward to build a multi-scale model which can be relevant at both molecular and device levels.

Chapter 6

Appendix

6.1 Appendix I: Algorithm for Solving Spreading Impedance Model

6.1.1 Matrix Method

To solve the equations used in our model we have used finite difference technique. For implementing the finite difference technique we have discretized the equations. The discretization of the equations 2.9-2.12 can be given as follows:

For dark or non-illuminated nodes, $m \in S_{NIL}$

$$I_s\left[exp\left(\frac{q\phi_m^t}{k_BT}\right)-1\right]+C_t\frac{\phi_m^{t+\Delta t}-\phi_m^t}{\Delta t}+ \sum_{l\in S_{IL}}\left[\frac{\phi_m^t-\phi_l^t}{R_{sp}(l,m)}+C_{sp}(l,m)\frac{(\phi_m^{t+\Delta t}-\phi_m^t)-(\phi_l^{t+\Delta t}-\phi_l^t)}{\Delta t}\right]=0 \tag{6.1}$$

For illuminated nodes, $l \in S_{IL}$,

$$I_s\left[exp\left(\frac{q\phi_l^t}{k_BT}\right)-1\right]+C_t\frac{\phi_l^{t+\Delta t}-\phi_l^t}{\Delta t}+I_{ph,l}+ \sum_{\substack{m\in S_N\\ m\neq l}}\left[\frac{\phi_l^t-\phi_m^t}{R_{sp}(l,m)}+C_{sp}(l,m)\frac{(\phi_l^{t+\Delta t}-\phi_l^t)-(\phi_m^{t+\Delta t}-\phi_m^t)}{\Delta t}\right]=0 \tag{6.2}$$

For the left electrode potential Φ_L,

$$N_LI_s\left[exp\left(\frac{q\Phi_L^t}{k_BT}\right)-1\right]+N_LC_t\frac{(\Phi_L^{t+\Delta t}-\Phi_L^t)}{\Delta t}+ \sum_{\substack{m\in S_{LE}\\ l\in S_{IL}}}\left[\frac{(\Phi_L^t-\phi_l^t)}{R_{sp}(m,l)}+C_{sp}(m,l)\frac{(\Phi_L^{t+\Delta t}-\Phi_L^t)-(\Phi_l^{t+\Delta t}-\Phi_l^t)}{\Delta t}\right]=0 \tag{6.3}$$

Similarly, for the right electrode potential Φ_R,

$$N_RI_s\left[exp\left(\frac{q\Phi_R^t}{k_BT}\right)-1\right]+N_RC_t\frac{(\Phi_R^{t+\Delta t}-\Phi_R^t)}{\Delta t}+ \sum_{\substack{m\in S_{LE}\\ l\in S_{IL}}}\left[\frac{(\Phi_R^t-\phi_l^t)}{R_{sp}(m,l)}+C_{sp}(m,l)\frac{(\Phi_R^{t+\Delta t}-\Phi_R^t)-(\Phi_l^{t+\Delta t}-\Phi_l^t)}{\Delta t}\right]=0 \tag{6.4}$$

These equations may be put in the matrix form as

$$AB=C \tag{6.5}$$

Where

$$A = \begin{pmatrix} \frac{C_t + C_{sp}(l,m)}{\Delta t} & 0 & 0 & \dots & \frac{C_s pl, m}{\Delta t} & \dots & 0 & 0 \\ 0 & \frac{C_t + C_{sp}(l,m)}{\Delta t} & 0 & \dots & \dots & \dots & 0 & 0 \\ \dots & \dots & \dots & \dots & \dots & \dots & \dots & \dots \\ \dots & \dots & \dots & \dots & \dots & \dots & \dots & \dots \\ 0 & 0 & 0 & \dots & \frac{C_{sp}(l,m)}{\Delta t} & \dots & 0 & \frac{C_t + C_{sp}(l,m)}{\Delta t} \end{pmatrix} \tag{6.6}$$

and

$$B = \begin{pmatrix} \Phi_L^{t+\Delta t} \\ \phi_{m_1}^{t+\Delta t} \\ \dots \\ \phi_l^{t+\Delta t} \\ \dots \\ \Phi_R^{t+\Delta t} \end{pmatrix} \tag{6.7}$$

$$C = - \begin{pmatrix} N_L I_s \left[exp\left(\frac{q\Phi_L^t}{k_B T}\right) - 1 \right] - N_L C_t \frac{\Phi_L^t}{\Delta t} + \left[\frac{(\Phi_L^t - \phi_l^t)}{R_{sp}(m,l)} - C_{sp}(m,l) \frac{\Phi_L^t - \Phi_l^t)}{\Delta t} \right] \\ I_s \left[exp\left(\frac{q\phi_{m_1}^t}{k_B T}\right) - 1 \right] - C_t \frac{\phi_m^t}{\Delta t} + \frac{\phi_{m_1}^t - \phi_l^t}{R_{sp}(l,m)} - C_{sp}(l,m) \frac{-(\phi_{m_1}^t + \phi_l^t)}{\Delta t} \\ \dots \\ I_s \left[exp\left(\frac{q\phi_l^t}{k_B T}\right) - 1 \right] - C_t \frac{\phi_l^t}{\Delta t} + I_{ph,l} + \left[\frac{\phi_l^t - \phi_m^t}{R_{sp}(l,m)} - C_{sp}(l,m) \frac{(\phi_l^t - \phi_m^t)}{\Delta t} \right] \\ \dots \\ N_L I_s \left[exp\left(\frac{q\Phi_L^t}{k_B T}\right) - 1 \right] - N_L C_t \frac{\Phi_L^t}{\Delta t} + \left[\frac{(\Phi_L^t - \phi_l^t)}{R_{sp}(m,l)} - C_{sp}(m,l) \frac{\Phi_L^t - \Phi_l^t)}{\Delta t} \right] \end{pmatrix} \tag{6.8}$$

Now by taking the inverse of A, we can get potential ($\phi(t)$) for each node and hence the LPV.

For taking the matrix inverse, we have used Intel Math Kernel Library subroutines.

6.1.2 Alternative Numerical Approach

Our alternative approach is based on the fact that all the potentials are related to $\phi_l(t)$. The discretization of the equations are done in the same way. Here we take all the terms with $t + \Delta t$ on the right side and rest of the terms are taken on the left side. All the other potentials at $t = 0$ are initially zero and then evolve along with illuminated node potential.

The algorithm is as following:

(i) Initializing all the potentials $\phi(t = 1)$ to be zero.

(ii) Solving $\phi_l(t = t + \Delta t)$.

(iii) Solving all the other potentials at $t = t + \Delta t$ using $\phi_l(t = 2)$.

(iv) Updating t and $\phi_l(t)$.

(v) Getting the LPV or desired node potential with time.

This algorithm doesn't involve any matrix inversion and henec is faster than previous one and can also deal with bigger lattice sizes. Thus, by this approach we have been able to do far more efficient and faster calculations.

6.2 Appendix II: Kinetic Monte Carlo Algorithm

The Monte Carlo Algorithm that we have used in chapter 4 is as follows:

(A) From Gaussian Random Number generator, random numbers are generated and distributed throughout the lattice. These random numbers are the energies of lattice points.

(B) The hopping rates for all possible destination from a particular site are calculated. It can be done for whole lattice or within a defined radius.

(C) The new destination is chosen according to hopping rate. The site with most imminent hopping rate is choose to be a new site.

(D)Sum of hopping times $\sum \Gamma_{ij}$ for the sites are calculated.

(E) A random number X is generated from uniform distribution.

(F) Time is updated according to

$$t_{new} = t_{old} - \ln \frac{X}{\sum \Gamma_{ij}} \tag{6.9}$$

(G) Velocity, the time of flight and mobilities are calculated and stored. For Gaussian Random Number Generator, Intel Math Kernel Subroutines have been used.

Chapter 7

Bibliography

1. N. Karl, Organic Semiconductors, O. Madelung, M. Schulz, and H. Weiss (Eds.), Landolt-Boernstein (New Series), Group III, Vol. 17 Semicondcuctors, Subvolume 17i, page 106. Springer, Berlin, 1985.

2. J. Koenigsberger, K. Schilling, Ann. Physik **32**, 179 (1910).

3. M. Volmer, Ann. Physik **40**, 775 (1913).

4. M. Pope, H. Kallmann, and P. Magnante, J. Chem. Phys. **38**, 2042 (1963).

5. H. Shirakawa, E. J. Louis, A. G. MacDiarmid, C. K. Chiang and A. J. Heeger, J.Chem. Soc. Chem. Commun. **16**, 578 (1977).

6. C. K. Chiang, C. R. Fincher, Jr., Y. W. Park, and A. J. Heeger, H. Shirakawa, E. J. Louis, S. C. Gau, and Alan G. MacDiarmid, Phys. Rev. Lett. **39**, 1098 (1977).

7. Ghosh A.K. et al. J.Appl.Phys. **45**,230-236 (1974).

8. Halls J.J.M., Friend R.H. In: Archer M.D., Hill R.D. editors, Clean electricity from photovoltaics, London: Imperial College Press, 377-445 (2001).

9. Halls J.J.M. et al. Nature **376**, 498-500 (1995).

10. Yu G. et al. Science **270**, 1789-1791 (1995).

11. Yu G. et al. Adv.Mat. **10**, 1431-1434 (1998).

12. Forrest S.R. Nature, **428**, 911-918 (2004).

13. H. Koezuka, A. Tsumura, T. Ando Synthetic Metals **18** 699-704(1987).

14. Aline Hepp, Holger Heil, Wieland Weise, Marcus Ahles, Roland Schmechel, and Heinz von Seggern Phys. Rev. Lett. **91**, 157406(2003).

15. T. Manaka, F. Liu, M. Weis and M. Iwamoto Phys. Rev. B **78**, 121302(2008).

16. Partridge, R . Polymer **24**, 755(1983).

17. Tang, C. W.; Vanslyke, S. A. Applied Physics Letters **51**, 913 (1987).

18. Burroughes, J. H., et al. Nature **347**, 539 (1990).

19. W. Brutting, Physics of Organic Semiconductors WILEY-VCH Verlag GmbH & Co. KGaA, Weinheim, 2005.

20. W. P. Su, J. R. Schrieffer, and A. J. Heeger, Phys. Rev. Lett.,**42**, 1698 (1979).

21. W. P. Su, J. R. Schrieffer, and A. J. Heeger Phys. Rev. B **22**, 2099 (1980).

22. W. P. Su and J. R. Schrieffer, Proc. Natl. Acad. Sci. USA, **77**, 5626 (1980).

23. J. L. Brdas, R. R. Chance, and R. Silbey, Mol. Cryst. Liq. Cryst.,**77**, 319 (1981).

24. P. G. Drazin and R. S. Johnson ,Solitons: an introduction. Cambridge University Press, 2nd ed(1989).

25. A. J. Heeger, S. Kivelson, J. R. Schrieffer, W. P. Su Rev. Mod. Phys. **60**, 781850 (1988).

26. J. L. Bredas and G. B. Street Acc. C hem. Res. ,**18**, 309-315 (1985).

27. Gregory D. Scholes and Garry Rumbles nature materials **5**,683, 2006.

28. W Y Liang Phys. Educ. **5** 226 (1970).

29. Glowe Jean-Francois et al, Physical review B **81**, 041201(R) (2010).

30. Demetrio A. da Silva Filho, et al. Chem. e Commun., 1702 (2004).

31. Roel S. Sanchez-Carrera, Veaceslav Coropceanu, Demetrio A. da Silva Filho, Rainer Friedlein, Wojciech Osikowicz, Richard, Christian Suess, William R. Salaneck, and Jean-Luc Bredas. J. Phy. Chem. B, **110**, 1890418911 (2006).

32. E.F. Valeev, V. Coropceanu, D.A. da Silva, S. Salman, and J.L. Bredas J. Am. Chem.Soc., **128(30)**, 9882 9886(2006).

33. V. Lemaur, et al J. Am. Chem. Soc., **126(10)**, 3271 3279 (2004).

34. J. Bredas, D. Beljonne, V. Coropceanu, and J. Cornil. Chem. Rev., **104(11)**, 4971 5003 (2004).

35. V. Coropceanu, J. Cornil, D. A. da Silva, Y. Olivier, R. Silbey, and J. L. Bredas. Chem. Rev.,**107(5)**,2165 2165(2007).

36. P. Hohenberg and W. Kohn, Phys. Rev. **136** B864 (1964).

37. Arfken Weber, Mathematical Methods for Physcicists, 5th edition, Elsevier

38. O. Bleibaum, H. Bottger, and V.V. Bryksin, Phys. Rev. B **54**, 5444 (1996).

39. S.R. Broadbent and J.M. Hammaresley, Proc. Camb, Phil. Soc. **53**, 629 (1957).

40. M.C.J.M. Vissenberg, S. Stallinga and G. Vertogen Physical Review E **55**,4367-4377 (1997).

41. H. Bassler, Phys. Status Solidi B **175**, 15(1993).

42. G. Schnherr, H. Bssler, M. Silver, Philos. Magz. **44** 47 (1981).

43. P. M. Borsenberger, L. Pautmeier, H. Bssler, J. Chem. Phys. **94** 5447 (1991).

44. V. Ambegaokar, B.I. Halperin, J.S.Langer, Phys. Rev. B **57**, 12964 (1998).

45. B. Mazhari, Solar Energy Materials and Solar Cells, **90**, Issues 7-8, 1021-1033, (2006).

46. D. Kabra, S. Shriram, N. S. Vidhyadhiraja, and K. S. Narayan J. Appl. Phys. **101**, 064510 (2007)

47. J. Burroughes et al, Nature **347**, 539 (1990).

48. D. Kabra, Th. B. Singh and K. S. Narayan, Appl. Phys. Lett. **85** 21 (2004).

49. Valasaki, L. M. Moreira, L. Micaroni and I. A. Hummelgen, J. Appl. Phys. bf 92 2035 (2002).

50. J. Campbell, D. D. C. Bradley, and H. Antoniadis, Appl. Phys. Lett. **79** 2133 (2001).

51. A. Choulis et al, Appl. Phys. Lett. **85** 3890 (2004).

52. A. Fynn, J. Bajaj, and L. Farone, IEEE Trans. Elect. Dev. **42** 1775-1782 (1995).

53. P. Keith Watson, IEEE Transaction on dielectrics and Electrical Insulation, **2**, 5, (1995).

54. Piet Van Mieghem, Probability in the Engineering and Informational Sciences, **15**, 535555, (2001).

55. Anssi Mkynen: Position-Sensitive Devices and Sensor Systems for optical Tracking and Displacement Sensing Application. Dissertation, Faculty of Technology, University of Oulu, (2000).

56. J. T. Wallmark: A new semiconductor photocell using lateral photoeffect. Proceedings of the IRE, **45**, S. 474-483, (1957).

57. Dinesh Kabra, J. Verma, N. S. Vidhyadhiraja and K. S. Narayan, IEEE Sensors Journal, **8**, 1663-1671 (2008).

58. V I Arkhipov , A V Vannikov , G S Mingaleev , Yu A Popova , A I Rudenko , V S Saenko and A P Tyutnev Journal of Physics D: Applied Physics, **17**, Number 7 (1984)

59. E. H. Bttcher, F. Hieronymi, D. Kuhl, E. Drge, and D. Bimberg Appl. Phys. Lett. **62**, 2227 (1993).

60. Kohkichi Konno, Osamu Matsushima, Kiyohito Hara, Gaku Suzuki, Dondee Navarro and Mitiko Miura-Mattausch Jpn. J. Appl. Phys. **44**, 2584-2585,(2005).

61. Robert A. MacLachlan and Cameron N. Riviere IEEE Transactions on Instrumentation and Measurement, **58**, 6, (2009)

62. R. Gordon, J. Chem. Phys. **48**, 1408 (1968).

63. F.F. Abraham and G.W. White, J. Appl. Phys. **41**, 1841 (1970).

64. C.S. Kohli and M.B. Ives, J. Crystal Growth **16**, 123 (1972).

65. G.H. Gilmer, J. Crystal Growth **35**, 15 (1976).

66. M. Bowker and D.A. King, Surf. Sci. **71**,583 (1978).

67. D.A. Reed and G. Ehrlich, Surf. Sci. **105**, 603 (1981).

68. P.A. Rikvold, Phys. Rev. **A 26**, 647 (1982).

69. E.S. Hood, B.H. Toby, and W.H. Weinberg, Phys. Rev. Lett. **55**, 2437 (1985).

70. S.V. Ghaisas and A. Madhukar, J. Vac. Sci. Technol. **B 3**, 540 (1985).

71. A.F. Voter, Phys. Rev. B **34**, 6819 (1986).

72. D.T. Gillespie. The Journal of Physical Chemistry, **81(25)**, 23402361 (1977).

73. G. Horowitz. Journal Of Materials Research, **19(7)**,19461962 (2004).

74. Z. Yu, D. Smith, A. Saxena, R. Martin, and A. Bishop Physical Review Letters, **84(4)**,721724 (2000).

75. Miller and E. Abrahams, Phys. Rev. **120**, 745 (1960).

76. Sze, Physics of Semiconductor Devices, 2nd edition, Section 7.3.4.

77. J. Frenkel, Phys. Rev., **54**, 647-648 (1938).

78. Joseph John Kwiatkowski PhD Thesis, From molecules to mobilities: modelling charge transport in organic semiconductors, Department of Physics, Imperial College (2008).

79. Pierls, Quantum Theory of Solids(Clarendon, Oxford) (1955).

80. http://www-oe.phy.cam.ac.uk University of Cambridge Organic Electronics group website.

81. Chapter 1, Soumya Dutta Thesis, CPMU, JNCASR.